

ISRN LUTFD2/TFME - 17/5034 - SE(1-62)

LUND UNIVERSITY

DIVISION OF MECHANICS

# Minimizing Cooling Time for Diamond Anvil Cell Under High Pressure

by Martin Edung

Supervisors:

Docent Aylin Ahadi, Division of Mechanics, LU  
Malcolm Guthrie, High Pressure Scientist, ESS

For more information:

Division of Mechanics, Lund University, Box 118,  
SE-211 00 Lund, Sweden

Copyright © 2017 by Martin Edung

Printed by Media-Tryck, Lund, Sweden

January 31, 2017



## Abstract

The main goal of the project was to decrease the cooling time of a diamond anvil cell (DAC) by modifying an existing design. Modifications included change of materials, overall dimensions and a significant reduction of mass together with additional suggestions for decreased cool time.

The initial design was known to function with current materials and dimensions. The first step of the thesis was to import the geometry, when applying the same force, but changing the materials (from Inconel to C17200 AT(TF00)) and locate high stress areas. Any part of the geometry that exceeded the yield criterion (with safety factor) was modified and tested in an iterative process until the criterion was satisfied. Material was removed in a similar iterative process in areas with very low stress concentrations. Finite element analysis was made with the commercial software Ansys WB. Stress analysis was carried out using Ansys WB Static Structural since the criterion did not allow any part to be out of the elastic regime. To get a sense of the decreased cooling time, a comparison between the original design and the modified design was made using Ansys WB Transient Thermal with the different geometries and materials. Material parameters (mechanical and thermal) was gathered from literature. Fatigue analysis was made by using an estimate of the RCC-MRx standard.

Apart from computational analysis, several alternations of the design was made to make it easier for manufacture and usage, together with complete machine drawings which can be viewed in the appendix.

The thesis resulted in a complete and modified structure which is within the elastic region with a safety factor of 1.2 (criteria), with an increase in diffraction aperture windows of 20 degrees (goal: up to 10 degrees) to fully capture emitting neutrons, an infinite life time against fatigue failure (goal: 500 cycles) and a total mass reduction of around 30%. The material, the dimensions and several parameters has been changed which resulted in a decreased cooling time of around 75% (goal: 10%), only by adjusting the Diamond Anvil Cell. By adjusting the Closed Cycle Refrigerator and the process of cooling the device, the cooling time could be even faster.

## **Acknowledgements**

I would like to thank Zvonko Lazic for introducing me to the ESS and always being a positive quanta of energy, Malcolm Guthrie for offering me the thesis and giving me an insight to the narrow world of DAC's, Emil Lundh and Jonathan Moberg for helping me understand commercial finite-element software in general and Ansys WB in specific and being aids for understanding the physics and numerics behind the results, and finally Aylin Ahadi from Lund University for being my academic supervisor.



# Contents

<b>1</b>	<b>Introduction</b>	<b>1</b>
1.1	The ESS . . . . .	1
1.2	Background . . . . .	1
1.3	Diamond Anvil Cell . . . . .	1
1.4	Closed Cycle Refrigerator . . . . .	4
1.5	Project goals . . . . .	4
1.6	Analysis tools and procedures for evaluation . . . . .	5
<b>2</b>	<b>Material data</b>	<b>6</b>
2.1	Thermal conductivity . . . . .	6
2.1.1	Copper . . . . .	6
2.1.2	Copper-Beryllium C17200 AT(TF00) . . . . .	6
2.1.3	Inconel 718 . . . . .	6
2.2	Specific Heat . . . . .	6
2.2.1	Copper and its alloys . . . . .	6
2.2.2	Inconel 718 . . . . .	7
2.3	Mechanical Properties . . . . .	7
2.3.1	Copper-Beryllium C17200 AT(TF00) . . . . .	7
2.3.2	Vascomax c350 . . . . .	8
2.3.3	Other materials . . . . .	9
<b>3</b>	<b>Theory</b>	<b>10</b>
3.1	Finite Element Formulation . . . . .	10
3.1.1	Transient Thermal . . . . .	10
3.1.2	Static Structural . . . . .	11
3.2	Fatigue . . . . .	13
<b>4</b>	<b>Method</b>	<b>15</b>
4.1	Simplifications . . . . .	15
4.2	Meshing . . . . .	15
4.3	Newton-Raphson algorithm . . . . .	17
4.4	Penalty formulation . . . . .	17
4.5	Detection points . . . . .	18
4.6	Weak Springs . . . . .	18
4.7	Time increment . . . . .	18
4.8	Fatigue . . . . .	19
4.9	Boundary Conditions Transient Thermal . . . . .	19
4.10	Boundary Conditions Static Structural . . . . .	20

<b>5</b>	<b>Results</b>	<b>20</b>
5.1	Structural Analysis of Initial Design . . . . .	20
5.2	Submodels of Structural Analysis . . . . .	20
5.3	Deciding Dimensions to Avoid Yield . . . . .	21
5.3.1	Bottom plate radius . . . . .	21
5.3.2	Thickness of Part 1 Lower Plate . . . . .	22
5.3.3	Filet Radius on Piston . . . . .	23
5.3.4	Width of diffraction window . . . . .	23
5.3.5	Filet Radii around Lip Surface . . . . .	24
5.3.6	Global Radius . . . . .	24
5.4	Results from improved design . . . . .	25
5.4.1	Stresses global geometry . . . . .	25
5.4.2	Stresses Modified Piston . . . . .	26
5.4.3	Stresses Modified Diffraction Aperture . . . . .	26
5.4.4	Fatigue . . . . .	27
5.5	Thermal Analysis . . . . .	31
5.5.1	Thermal Analysis of Initial Design . . . . .	31
5.5.2	Thermal Analysis of Modified Design . . . . .	31
<b>6</b>	<b>Validation</b>	<b>33</b>
6.1	Validating Mesh . . . . .	33
6.2	Extra Validations . . . . .	35
<b>7</b>	<b>Discussion</b>	<b>36</b>
	<b>Appendices</b>	<b>41</b>
	<b>Appendix A Machine Drawings of DAC</b>	<b>41</b>

## List of Figures

1	Isometric view and cut section view of the DAC with the CCR with colors to clearly show different parts of the product. . . . .	2
2	Different views of Diamond Anvil Cell referred to in this report. . . . .	3
3	Thermal conductivity over temperature for the different materials used in thermal analysis. . . . .	7
4	Scheme illustrating different ways to reach low temperature and high pressure. The DAC should be able to handle both paths. . . . .	8
5	Global element distribution concerning aspect ratio, skewness and elemental quality. . . . .	16
6	Illustration of pinball radius and penalty formulation. Pinball radius on figure (a) show the contact search size, and figure (b) show penetration distance denoted $x_p$ , and normal force denoted $F_n$ . . . . .	18

7	Detection points used for the penalty function. . . . .	18
8	Weak springs [N/mm] vs. force reaction of the global system. Smaller spring stiffness results in smaller reaction forces. . . . .	19
9	Global stress distribution of initial design. Figure (a) display stress distribution within seats, diamonds and elemental configuration. Figure (b) display interesting areas for modifications. Legend displays stress values in [MPa]. . . . .	21
10	Closer look at high stress area (rectangle 2 in figure 9). Figure (b) show singularity shown from below to illustrate nodal connection of elements, and (c) show peak stresses plotted against mesh refinement around edges of screw hole. Legend displays stress values in [MPa]. . . . .	22
11	Added thickness and its correlation to maximum stresses of part. With criterion stated earlier, a max stress of 800 MPa is allowed for all parts of BeCu, meaning a minimum thickness of lower part is somewhere around 7.5 mm. With added material, buckling is avoided, and the steel seat is in contact with a larger surface BeCu. . . . .	23
12	The lip surface was initially increased from 1 mm to 6 mm and a variety of radii for each part and was investigated with the 800 MPa-criterion to avoid yield stress with a safety factor of 1.2. . . . .	24
13	Cut section of DAC displaying stress distribution. Legend displays stress values in [MPa]. . . . .	25
14	Quarter symmetry of piston displaying stress distribution. Red colors show areas exceeding yield criterion. The initial design of the piston had stresses beyond yield criterion, and the modified version had stresses within yield criterion (maximum stresses of modified piston: 496 MPa). . . . .	26
15	Quarter symmetry of piston displaying stress distribution. The initial design had stresses beyond yield criterion on several places, and the modified version had stresses all within yield criterion. Legend shows stresses in [MPa] . . . . .	27
16	Linearized stresses along a defined path (see <i>figure a</i> ) in the diffraction aperture, used for fatigue analysis. Legend displays peak stresses (red), membrane and bending stresses (yellow) and total stresses (blue). . . . .	29
17	Linearized stresses along a defined path (see <i>figure a</i> ) in the base part, used for fatigue analysis. Legend displays peak stresses (red), membrane and bending stresses (yellow) and total stresses (blue). . . . .	30
18	Temperature distribution in intervalls of 500 seconds for the initial design. Images displaying half symmetry of DAC with CCR. Dark blue color represents 4K, and red represents 295.15K. . . . .	31
19	Temperature distribution in intervalls of 500 seconds for the modified, improved design. Images displaying half symmetry of DAC with CCR. Dark blue color represents 4K, and red represents 295.15K. . . . .	32
20	Temperatures time-dependency for diamonds in initial- and modified design. . . . .	33

21	Mesh refinement and corresponding maximum stresses for each part. Figure (d) is referring to part 2 and 3. . . . .	34
22	Rendered image of the finished product. . . . .	38

## List of Tables

1	Copper Beryllium alloy C17200, and its elements in mass percent . . .	2
2	Parts of the DAC with its mass in total and relative numbers, arranged according to mass. The part numbers are referred to figure 2b. . . . .	4
3	Thermal conductivity over temperature for regular BeCu, and a comparison value for alloy C17200 (not treated) [3], [12]. . . . .	6
4	Comparison between specific heat values of Inconel and Nickel in a region with overlapping data. . . . .	7
5	Mechanical properties of C17200 AT(TF00) at room temperature [6]. .	8
6	Mechanical properties of C17200 AT(TF00) at room temperature. . . .	8
7	Each part modeled and its given elemental size. . . . .	15
8	Mesh criteria with its average value, standard deviation and failed elements (total number of elements that is not within the above mentioned criteria). . . . .	16
9	Discrete temperature values for diamonds in initial and modified design over time. . . . .	32
10	Reaction forces for contact surfaces (given notation contact/target), and its difference to reference value in percent. . . . .	35

# 1 Introduction

## 1.1 The ESS

The European Spallation Source (ESS) is one of the worlds largest science and technology facilities being built today, involving 17 European countries with a total budget of almost 2G€. It will involve the worlds most powerful proton accelerator, a four tonne helium cooled target wheel in tungsten, 22 cutting edge neutron instruments, several laboratories and a supercomputing data management and software development center.

The ESS will be the world's most powerful neutron source, far brighter than today's leading neutron facilities with up to 100 times the neutron beam intensity. The neutrons are released through spallation of tungsten, initiated by pulses of accelerated protons colliding with a rotating wheel of tungsten. Emitted neutrons are led via beam lines to experimental stations equipped with advanced instruments to analyze the samples. The facility will be a multi-disciplinary research centre useful for deeper understanding of pharmaceuticals, plastics, engines, proteins molecules, nanotechnology and more.

## 1.2 Background

The ESS will be accessed solely to researchers performing experiments with interest to science and technology not capable by other facilities. If permitted, researchers will only be able to access the neutron beam facility 3-10 days per year for a cost of 30k€ per day. When these measurements are made at low temperatures and high pressures, the total amount of beam time can be significantly reduced due to the time of cooling and heating of samples. With the current configuration, cooling the pressurizing device takes almost eight hours (from room temperature to 4K), which reduces the total amount of available beam time significantly. The subject of this report is to investigate ways to decrease the time of cooling of this specific device called a Diamond Anvil Cell.

## 1.3 Diamond Anvil Cell

Diamond anvil cells (DAC) can be used to obtain high pressure samples by compressing a sample between two culets of a hard incompressible material, such as diamond. The sample is fixed between the culets using a ductile metallic gasket that will plastically deform upon loading, thus making it hard for the sample to escape pressurization.

Neutrons enter through the bottom of the cell, enters the diamonds and the sample, and exits through the top of the cell and through the aperture windows on the sides. The diffracted neutrons are captured by detectors and are the base for research.

The original device, before modifications made in this report, consisted of two opposed diamonds, upheld by rings of sintered diamond (first ring), tungsten carbide (second

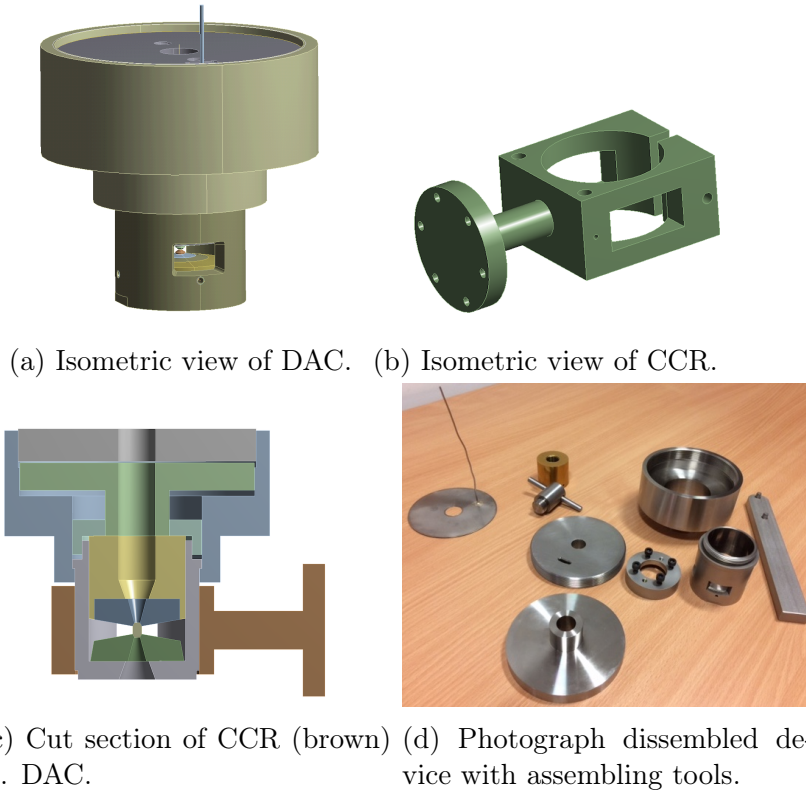


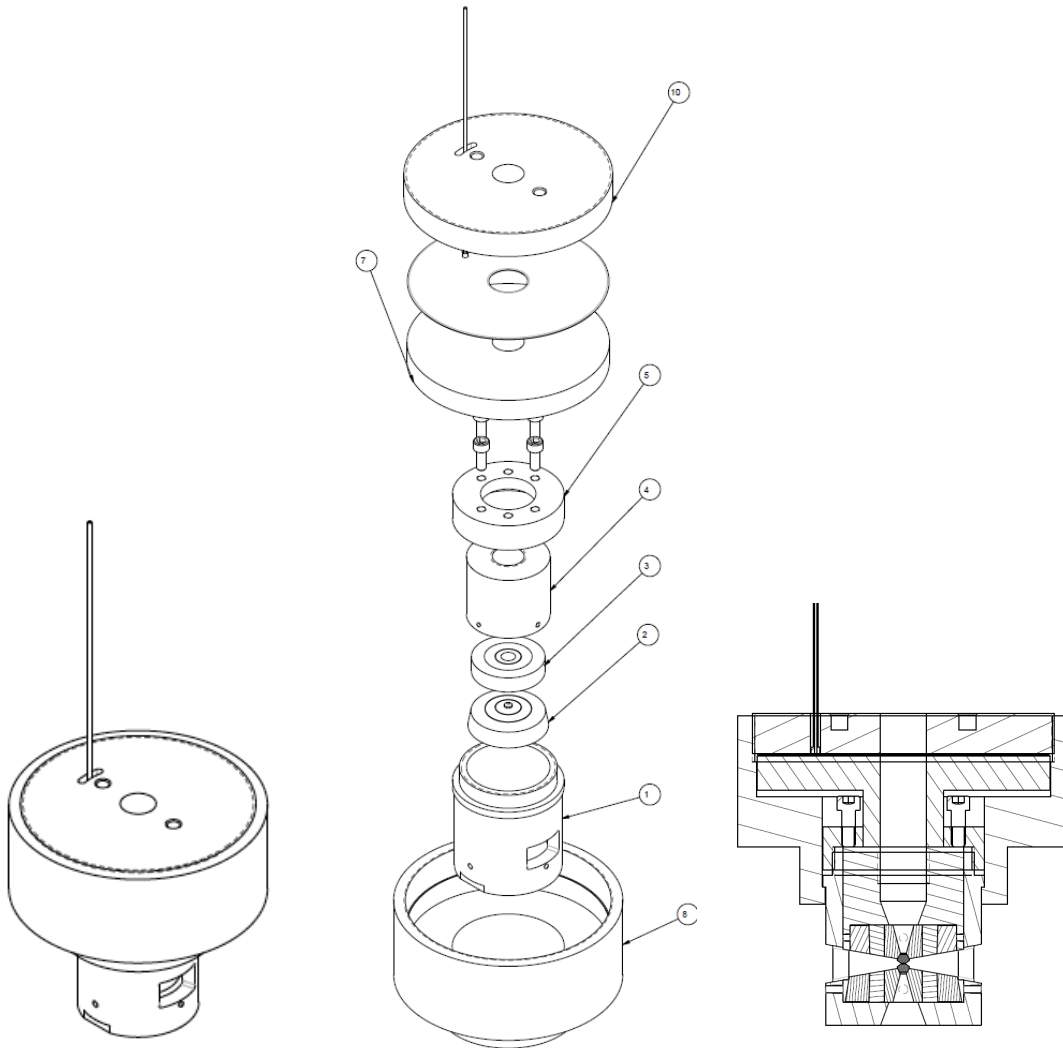
Figure 1: Isometric view and cut section view of the DAC with the CCR with colors to clearly show different parts of the product.

ring) and steel (third ring). The remaining parts were made of a Nickel-based alloy called Inconel 718. In the report, Inconel 718 will be substituted to a heat treated and precipitation hardened copper alloy, C17200 AT(TF00) an alloy with better thermal properties. The rings upholding the diamonds will be replaced by a steel, Vascomax c350 and the diamonds will be replaced with bigger diamonds.

The copper alloy C17200 AT(TF00) is a Copper-Beryllium made from the materials shown in table 1.

Table 1: Copper Beryllium alloy C17200, and its elements in mass percent

Element	Mass%
Be	1.80-2.00
Co + Ni	0.20-0.50
Fe	0.1 (max)
Cu	<i>balance</i>



(a) Isometric view.

(b) Exploded view.

(c) Section view.

Figure 2: Different views of Diamond Anvil Cell referred to in this report.

An inflatable plate (the plate between the threaded lid and the piston in figure (2b)) consists of two circular discs welded together by its inner and outer radius. Through a straw-shaped metal tube, pressurized helium gas expands the plate causing it to elastically deform to the shape of a torus. This deformation cause great forces on a threaded lid and a vertically translatable piston, which in turn cause forces on the spacer, seats and diamonds which generates a high pressure sample. The benefit of this solution is its capability to adjust pressure at any time during the experiment by simply adjusting the gas flow, without having to heat up and disassemble the device.

Table 2: Parts of the DAC with its mass in total and relative numbers, arranged according to mass. The part numbers are referred to figure 2b.

Name	Part Number	Mass (kg)	mass%
Diffraction Aperture	1	0.475	9.7
Spacer	4	0.292	6.0
Screw Holder	5	0.152	3.1
Piston	7	0.836	17
Base Part	8	1.89	38.6
Threaded Lid	10	0.943	19.2
rest	-	0.3	6.1
$\Sigma$	-	4.9	100

Part 2 and 3 in figure (2b) are denoted *seats*, and the *inflatable plate* is the part between part 7 and 10.

## 1.4 Closed Cycle Refrigerator

The Closed Cycle Refrigerator (CCR) is shown in figure (1b), and is purely made of copper. The CCR decreases the temperature of the DAC through convection, surface to surface. The CCR itself is cooled through the end plate which is bolted to a cooling device, a process not considered in this report.

## 1.5 Project goals

The goals of the project are as follows:

- Minimize time for cooling and heating by 10-15%
- Safety factor 1.2 against plasticity under 10 tonne load
- If possible, increase diffraction aperture of the cells, removing un-needed material in these regions
- A total life of at least 500 cycles before fatigue failure



Reconstructing the cell will include the use of diamonds with other dimensions, the use of Copper-Beryllium instead of Inconel, EU standards instead of U.S. standards and seats made out of steel instead of the previously used composite rings. To clarify: a 10 tonnes load is acting on each surface causing a 2x10 tonnes load in total.

## **1.6 Analysis tools and procedures for evaluation**

The finite element analysis was carried out using Ansys WB for stress and thermal analysis. For stress analysis, static structural was used since the DAC is intended to be within the elastic region. For thermal analysis, transient thermal was used to fully capture time dependency of cooling. Stress analysis was used in an iterative process, for several slightly modified designs. Thermal analysis was used for the initial and final design to evaluate how the project has fulfilled the project goals. Material data was imported from literature to Ansys Engineering Data manually, since there was no database available in Ansys for BeCu C17200 AT(TF00). Fatigue analysis was made using an estimate of AFCEN's RCC-MRx standard, and machine drawing was made using CATIA v6.

## 2 Material data

Material data differ for certain parameters in the wide temperature range for this application (4-300K). With this specific alloy and treatment, there is not much material data for low temperatures. Values for thermal conductivity are for regular Copper-Beryllium, and specific heats are assumed to be similar to values for normal Copper.

### 2.1 Thermal conductivity

#### 2.1.1 Copper

Copper is used for the CCR and its thermal conductivity,  $k$ , is based on the formula given below [8]

$$\log(k) = \frac{2.2154 - 0.88068T^{0.5} + 0.29505T - 0.048310T^{1.5} + 0.003207T^2}{1 - 0.47461T^{0.5} + 0.13871T - 0.020430T^{1.5} + 0.001281T^2} \quad (1)$$

which acts according to figure (3a) .

#### 2.1.2 Copper-Beryllium C17200 AT(TF00)

Copper-Beryllium is used for almost all parts (except seats and CCR). Values for this alloy and this treatment are approximated to regular beryllium-copper (not treated) using discrete values for different temperatures and curve fitted accordingly to figure (3b) [3]. A comparison value for the right alloy (not treated) is given in table (3) to give an estimate of the accuracy of the approximation.

Table 3: Thermal conductivity over temperature for regular BeCu, and a comparison value for alloy C17200 (not treated) [3], [12].

Temperature [K]	10	20	50	100	200	300
BeCu [Wm-1K-1]	5.1	10.3	24	44.5	79.5	112
C17200 [Wm-1K-1]	-	-	-	-	-	105

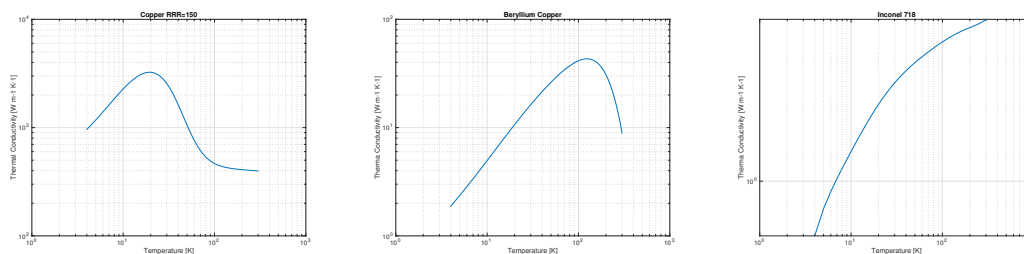
#### 2.1.3 Inconel 718

Thermal conductivity is given by formula and parameters from [8] (same as equation (1), but with different parameters), which is shown in figure (3c).

## 2.2 Specific Heat

### 2.2.1 Copper and its alloys

Temperature dependent values for specific heat for copper were found in tabular values between temperatures 1-300K [5], and are approximated to be the same for copper alloys.



(a) Anti-oxidized copper      (b) Copper Beryllium      (c) Inconel 718

Figure 3: Thermal conductivity over temperature for the different materials used in thermal analysis.

### 2.2.2 Inconel 718

Specific heat values for Inconel 718 are based on the formula and parameters stated in [16] for the temperature range  $T = 100 - 300K$ . In the range  $T = 4 - 100K$ , values for Inconel 718 are approximated to values of Nickel (Inconel is a Nickel-based alloy) based on [5]. Table 4 suggests the approximation to Nickel is a reasonable approximation, when comparing values in a region with overlapping data.

Table 4: Comparison between specific heat values of Inconel and Nickel in a region with overlapping data.

Temperature [K]	Inconel [W m <sup>-1</sup> K <sup>-1</sup> ]	Nickel [W m <sup>-1</sup> K <sup>-1</sup> ]	$\Delta\%$
100	232	232	0.0
120	275	278	1.0
140	311	314	1.0
160	340	342	0.6
180	362	365	0.8
200	378	383	1.3
220	393	397	1.1
240	405	410	1.2
260	415	422	1.6
280	423	433	2.3
300	432	445	3

## 2.3 Mechanical Properties

### 2.3.1 Copper-Beryllium C17200 AT(TF00)

Material data at room temperature for C17200 AT(TF00) are given by the table below. Heat treated, precipitation hardened BeCu is known to get stronger at lower temperatures [15]. The material should be designed to handle pressure at both room temperature and lower temperatures, which means material data for room temperature

would be the limiting factor. This is due to the fact that the samples being examined can act differently depending on its path to low temperature and high pressure, see figure (4).

Table 5: Mechanical properties of C17200 AT(TF00) at room temperature [6].

Properties	Value
Yield Strength	965-1207 MPa
Tensile Strength	1137-1380 MPa
Young's Modulus	131 GPa
Poisson's ratio	0.30

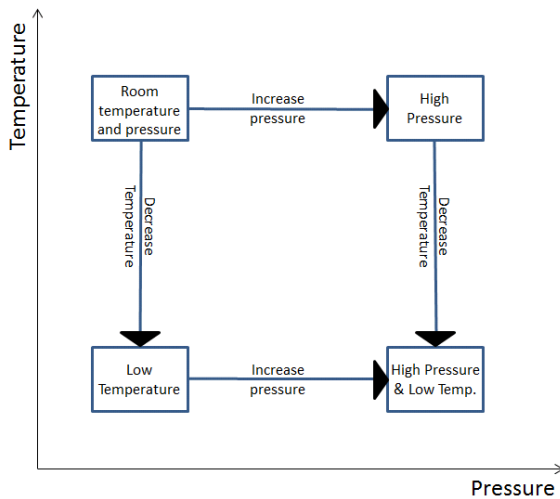


Figure 4: Scheme illustrating different ways to reach low temperature and high pressure. The DAC should be able to handle both paths.

### 2.3.2 Vascomax c350

The material used for the seats (part 2 and 3) will be Vascomax c350, which is a steel. Material parameters are according to the table below

Table 6: Mechanical properties of C17200 AT(TF00) at room temperature.

Properties	Value
Yield Strength	2344 MPa
Tensile Strength	2413 MPa
Young's Modulus	200 GPa
Poisson's ratio	0.30

### **2.3.3 Other materials**

Mechanical properties for structural steel is already given in Ansys, and no external data is inserted. Diamonds are approximated to be isotropic and are modeled using only Young's modulus and Poisson's ratio.

## 3 Theory

### 3.1 Finite Element Formulation

#### 3.1.1 Transient Thermal

Stationary heat flow is given by [11]

$$-\nabla \mathbf{q} + Q + \alpha(T - T_\infty) = 0 \quad (2)$$

Where  $\mathbf{q}$  is heat flux,  $Q$  is internal heat generation and the last term is Newton's boundary condition for convection. This function is multiplied with an arbitrary weight function and integrated over the body volume to

$$-\int_V v \nabla \mathbf{q} dV + \int_V v Q dV + \int_v v \alpha (T - T_\infty) dV = 0 \quad (3)$$

Using  $\mathbf{q} = -\mathbf{D} \nabla T$ ,  $\mathbf{q}^T \mathbf{n} = \mathbf{q}_n$  and Green-Gauss divergence theorem together gives

$$\int_V (\nabla v)^T \mathbf{D} \nabla T dV + \int_{S_g} v q_n dS - \int_{S_h} v h dS + \int_V Q dV + \int_v v \alpha (T - T_\infty) dV = 0 \quad (4)$$

This equation is solved using a Taylor-expansion of the temperature

$$T(x, y, z) = \begin{bmatrix} 1 & x & y & z \end{bmatrix} \begin{bmatrix} \alpha_1 \\ \alpha_2 \\ \alpha_3 \\ \alpha_4 \end{bmatrix} = \bar{\mathbf{N}} \alpha \quad (5)$$

For a specific element  $\mathbf{a}^e$  the following set of equations is obtained

$$\mathbf{a}^e = \begin{bmatrix} 1 & x_i & y_i & z_i \\ 1 & x_j & y_j & z_j \\ 1 & x_k & y_k & z_k \end{bmatrix} \begin{bmatrix} \alpha_1 \\ \alpha_2 \\ \alpha_3 \\ \alpha_4 \end{bmatrix} = \mathbf{C} \alpha \quad (6)$$

Equation 6 inserted in equation 5 results in the following relation

$$T^e = \bar{\mathbf{N}} \mathbf{C}^{-1} \mathbf{a}^e = \mathbf{N}^e \mathbf{a}^e \quad (7)$$

The gradient of equation 7 is given by

$$\nabla T^e = \begin{bmatrix} \frac{\partial N^e}{\partial x} \\ \frac{\partial N^e}{\partial y} \\ \frac{\partial N^e}{\partial z} \end{bmatrix} \mathbf{a}^e = \begin{bmatrix} \frac{\partial N_1^e}{\partial x} & \frac{\partial N_2^e}{\partial x} & \frac{\partial N_3^e}{\partial x} \\ \frac{\partial N_1^e}{\partial y} & \frac{\partial N_2^e}{\partial y} & \frac{\partial N_3^e}{\partial y} \\ \frac{\partial N_1^e}{\partial z} & \frac{\partial N_2^e}{\partial z} & \frac{\partial N_3^e}{\partial z} \end{bmatrix} \mathbf{a}^e = \mathbf{B}^e \mathbf{a}^e \quad (8)$$

The global set of equations are obtained by adding the individual elements to the following system

$$\nabla T = \mathbf{B}\mathbf{a} = \begin{bmatrix} \frac{\partial N_1^e}{\partial x} & \frac{\partial N_2^e}{\partial x} & \cdots & \frac{\partial N_n^e}{\partial x} \\ \frac{\partial N_1^e}{\partial y} & \frac{\partial N_2^e}{\partial y} & \cdots & \frac{\partial N_n^e}{\partial y} \\ \frac{\partial N_1^e}{\partial z} & \frac{\partial N_2^e}{\partial z} & \cdots & \frac{\partial N_n^e}{\partial z} \end{bmatrix} \begin{bmatrix} T_1 \\ T_2 \\ \vdots \\ T_n \end{bmatrix} \quad (9)$$

Equation 9 is inserted in equation 4 which results in

$$\int_v (\nabla v)^T \mathbf{D}\mathbf{B}dV \mathbf{a} = - \int_{Sh} v h dS - \int_{Sg} v q_n dS - \int_v v Q dV - \int_{Sc} v \alpha (\mathbf{N}\mathbf{a} - T_\infty) \quad (10)$$

The arbitrary weight function  $v$  is assigned using the Galerkin method, obtaining

$$v = \mathbf{N}\mathbf{c} \quad (11)$$

Where  $\mathbf{N}$  is the element shape functions. The weight function is equal to its transponent ( $v = \mathbf{N}\mathbf{c} = \mathbf{c}^T \mathbf{N}^T = v^T$ ), a particularity that will be used later.  $\mathbf{c}$  being arbitrary allows it to be eliminated from the function. Re-writing equation 10 results in

$$\begin{aligned} & \left( \int_v \mathbf{B}^T \mathbf{D}\mathbf{B}dV + \int_{Sc} \alpha \mathbf{N}^T \mathbf{N} dS \right) \mathbf{a} = \\ & = - \int_{Sh} \mathbf{N}^T h dS - \int_{Sg} \mathbf{N}^T q_n dS - T_\infty \int_{Sc} \mathbf{N}^T \alpha dS - \int_V \mathbf{N}^T Q dV \end{aligned} \quad (12)$$

Equation 12 is expressed as

$$(\mathbf{K} + \mathbf{K}_c) \mathbf{a} = \mathbf{f}_b + \mathbf{f}_l \quad (13)$$

Where the three surface integrals  $Sh$ ,  $Sg$ ,  $Sc$  are denoted as the boundary vector load  $\mathbf{f}_b$  and the heat generated by from the body is denoted  $\mathbf{f}_l$ . The stiffness matrices are denoted  $\mathbf{K}$  and  $\mathbf{K}_c$ , and the nodal displacements are denoted  $\mathbf{a}$

### 3.1.2 Static Structural

The differential equation for a three dimensional system in equilibrium is given by [11]

$$\tilde{\nabla}^T \boldsymbol{\sigma} + \mathbf{b} = 0 \quad (14)$$

Which in matrix format is expressed as

$$\begin{bmatrix} \frac{\partial}{\partial x} & 0 & 0 & \frac{\partial}{\partial y} & \frac{\partial}{\partial z} & 0 \\ 0 & \frac{\partial}{\partial y} & 0 & \frac{\partial}{\partial x} & 0 & \frac{\partial}{\partial z} \\ 0 & 0 & \frac{\partial}{\partial z} & 0 & \frac{\partial}{\partial x} & \frac{\partial}{\partial y} \end{bmatrix} \begin{bmatrix} \sigma_{xx} \\ \sigma_{yy} \\ \sigma_{zz} \\ \sigma_{xy} \\ \sigma_{xz} \\ \sigma_{yz} \end{bmatrix} + \begin{bmatrix} b_x \\ b_y \\ b_z \end{bmatrix} = \mathbf{0} \quad (15)$$

Cauchy's formula is applied as a boundary condition, relating the traction vector acting on the surface to the stresses of the body  $\mathbf{t} = \mathbf{S}\mathbf{n}$  which in x-direction is expressed as

$$t_x = \sigma_{xx}n_x + \sigma_{xy}n_y + \sigma_{xz}n_z \quad (16)$$

Equation 14 is multiplied with an arbitrary vector  $\mathbf{v}$  and integrated over the volume. The following is obtained in x-direction

$$\int_V v_x \frac{\partial \sigma_{xx}}{\partial x} dV + \int_V v_x \frac{\partial \sigma_{xy}}{\partial y} dV + \int_V v_x \frac{\partial \sigma_{xz}}{\partial z} dV + \int_V v_x b_x dV \quad (17)$$

Integrating by parts using Green-Gauss theorem, together with the expression for the traction vector in x-direction ( $t_x = \sigma_{xx}n_x + \sigma_{xy}n_y + \sigma_{xz}n_z$ ) results in

$$\int_S v_x t_x dS - \int_V \left( \frac{\partial v_x}{\partial x} \sigma_{xx} + \frac{\partial v_x}{\partial y} \sigma_{xy} + \frac{\partial v_x}{\partial z} \sigma_{xz} \right) dV + \int_V v_x b_x dV = 0 \quad (18)$$

Which added together in remaining dimensions of space, and formulated in compact format yields the following weak form of eq. 14

$$\int_V (\tilde{\nabla} v)^T \boldsymbol{\sigma} dV = \int_S \mathbf{v}^T \mathbf{t} dS + \int_V \mathbf{v}^T \mathbf{b} dV \quad (19)$$

We can introduce elasticity to the model by using the displacements as  $\mathbf{u} = \mathbf{N}\mathbf{a}$ , and choosing the Galerkin method for the weight function  $\mathbf{v} = \mathbf{N}\mathbf{c}$ , where  $\mathbf{v}$  and  $\mathbf{c}$  are arbitrary, and  $\mathbf{N}$  being the shape functions. These relations together with  $\tilde{\nabla} \mathbf{v} = \mathbf{B}\mathbf{c} = \tilde{\nabla} \mathbf{N}$  are added to the weak form (eq. 19) to

$$\int_V \mathbf{B}^T \boldsymbol{\sigma} dV = \int_S \mathbf{N}^T \mathbf{t} dS + \int_V \mathbf{N}^T \mathbf{b} dV \quad (20)$$

The constitutive model for thermoelasticity is  $\boldsymbol{\sigma} = \mathbf{D}(\boldsymbol{\epsilon} - \boldsymbol{\epsilon}_0)$ , where  $\boldsymbol{\epsilon}_0$  is the strains from the thermal analysis.  $\boldsymbol{\epsilon}$  is a vector containing normal- and shear strains, given by the relation  $\boldsymbol{\epsilon} = \tilde{\nabla} \mathbf{u} = \mathbf{B}\mathbf{a}$  using earlier stated relations. The constitutive model can now be expressed as

$$\boldsymbol{\sigma} = \mathbf{D}(\mathbf{B}\mathbf{a} - \boldsymbol{\epsilon}_0) \quad (21)$$

Which together with eq. 20 holds



$$\int_V (\mathbf{B}^T \mathbf{D} \mathbf{B} dV) \mathbf{a} = \int_S \mathbf{N}^T \mathbf{t} dS + \int_V \mathbf{N}^T \mathbf{b} dV + \int_V \mathbf{B}^T \mathbf{D} \boldsymbol{\epsilon}_0 dV \quad (22)$$

Equation 22 can be expressed as

$$\mathbf{K} \mathbf{a} = \mathbf{f}_b + \mathbf{f}_l + \mathbf{f}_0 = \mathbf{f} \quad (23)$$

The traction vector  $\mathbf{t} = \mathbf{S} \mathbf{n}$  is known along the surface  $Sh$  where it is denoted  $\mathbf{t} = \mathbf{h}$ , and the displacements  $\mathbf{u}$  are known along surface  $Sg$ . The surface integral can be re-formulated as  $\int_S \mathbf{N}^T \mathbf{t} dS = \int_{Sh} \mathbf{N}^T \mathbf{h} dS + \int_{Sg} \mathbf{N}^T \mathbf{t} dS$ .

### 3.2 Fatigue

RCC-MRx standard [13] is used within the elastic region, with neglected creep and irradiation because of sufficiently low temperatures. Notations in this segment is referring to the standard. Membrane stress,  $\sigma_m$ , [RCC-MRx RB 3224.13] and bending stresses,  $\sigma_b$  [RCC-MRxRB 3224.14] and peak stresses,  $P$ , are obtained by adding a *linearized stress intensity* to several defined paths (straight lines between two points i space) in regions of interest. Two secondary ratios,  $SR$  are obtained using

$$SR_1 = \frac{\Delta Q}{\sigma_{m,max}} \sim 0 \quad (24)$$

and

$$SR_2 = \frac{\Delta Q}{(\sigma_L + \sigma_b)_{max}} \sim 0 \quad (25)$$

hence the secondary stress for such low temperature gradients can be assumed as  $\Delta Q \sim 0$  [RCC-MRx RB 3261.111]. These values are compared to table values of [RCC-MRx RB 3261.1115] obtaining values  $v_1 = v_2 = 1$ , which are used to obtain

$$P_1 = \frac{\sigma_{m,max}}{v_1} \quad (26)$$

$$P_2 = \frac{(\sigma_L + \sigma_b)_{max}}{v_2} \quad (27)$$

$P_1$  and  $P_2$  are used in the following criteria, making sure progressive fatigue is avoided, a requisite for elastic fatigue analysis.

$$P_1 \leq 1.3 S_m \quad (28)$$

$$P_2 \leq 1.3 \cdot 1.5 S_m \quad (29)$$

Where  $S_m$  is defined as the minimum of [RCC-MRx A3.GEN.22].

The total strain is defined as

$$\overline{\Delta\epsilon_t} = \overline{\Delta\epsilon_1} + \overline{\Delta\epsilon_2} + \overline{\Delta\epsilon_3} + \overline{\Delta\epsilon_4} \quad (30)$$

Where  $\overline{\Delta\epsilon_1}$  is the elastic strain and the rest are different segments of plastic strains. The strains are given by

$$\overline{\epsilon_1} = \frac{2(1+\nu)}{3E} \overline{\Delta\sigma_{tot}} \quad (31)$$

$$\overline{\epsilon_2} = \frac{2(1+\nu)}{3E} \frac{\sigma_t}{100} \left(\frac{\Delta\sigma_t}{K}\right)^{1/m} \quad (32)$$

$$\overline{\epsilon_3} = (K_\epsilon - 1)\overline{\epsilon_1} \quad (33)$$

$$\overline{\epsilon_4} = (K_\nu - 1)\overline{\epsilon_1} \quad (34)$$

Where  $\sigma_t$  is given by

$$\sigma_t = \Delta[\sigma_m + 0.67(\sigma_b + P_L - \sigma_m)] \quad (35)$$

Where  $P_L = \sigma_m + L_m$  and  $L_m = 0$  for geometrical continuities.  $\overline{\Delta\sigma_{tot}}$  is given by

$$\overline{\Delta\sigma_{tot}} = \Delta(P + Q + F) \quad (36)$$

## 4 Method

### 4.1 Simplifications

For structural analysis a quarter symmetry of the DAC was modeled using two orthogonal symmetry planes, cutting the middle of the diffraction window of part 1. For transient analysis only one symmetry plane was used in order to fully capture heat flow through the geometry of the CCR. Symmetry planes are made to reduce the number of elements and consists of simply adding a frictionless contact to symmetry planes which is a non-linear, which is a non-linear, unilateral contact that allows for separation and a zero coefficient of friction.

Several parts were suppressed. The inflatable plate was replaced with uniform static pressure boundary condition acting on its contacting parts. Also the straw-shaped metal tube and two screws were suppressed because considered un-needed for analysis. Screws holding the seats in place (part 2 and 3 in figure (2b)) were simplified to cylinders of structural steel, with the purpose to capture stresses around the screws, and to be used as boundary conditions for holding the seats in place.

To reduce the total number of contact areas, the piston and the spacer (part 7 and 4 in figure (2b)) were modeled as one part, since it is made of the same material and is only pressurized in one direction. The two diamonds and the sample was modeled as one diamonds, which reduced two contact areas. The sample was very small, and would be very cost-ineffective to fully capture a 20 tonnes load with a few elemental thicknesses over a 0.05 mm sample and use comparable mesh sizes between parts.

Highly anisotropic diamonds are modeled using an isotropic model with appropriate strength.

Thermal analysis is not connected to structural analysis, which is a simplification of reality, which is justified due to the very slow cooling assumed to cause very low thermal stresses.

### 4.2 Meshing

All parts are meshed using tetrahedral elements, in order to fully capture geometrical irregularities, and for contact surfaces to have appropriate mesh connections. Master/slave mesh connections were applied on contact surfaces experiencing high pressure. To avoid discontinuities in stress distribution between parts of different mesh sizes, mesh refinements were added to contact surfaces with lower mesh sizes. Mesh refinements creates a denser mesh in the applied area with the thickness of a few elements. The global mesh consisted of 1 690 391 tetrahedron elements.

Table 7: Each part modeled and its given elemental size.

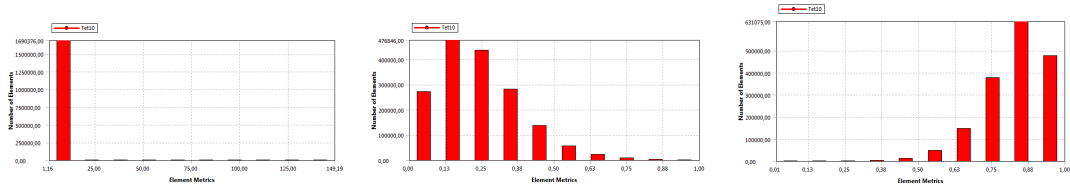
Part	Element size [mm]
Diffraction Aperture	0.8
Lower Seat	0.6
Upper Seat	0.6
Spacer	0.9
Screw Holder	1
Piston	0.9
Base Part	0.8
Threaded Lid	0.8
Screws	0.8
Diamonds	0.15
Total nbr	1 690 391 elm

Criteria for mesh was

- Aspect Ratio for tetrahedrons  $AR < 20$
- Corner angle  $60^\circ < \alpha < 160^\circ$
- Skewness  $< 0.9$

Table 8: Mesh criteria with its average value, standard deviation and failed elements (total number of elements that is not within the above mentioned criteria).

Criteria	Avrg	St Dev	Nbr failed
AR	1.87	0.52	2
Skewness	0.24	0.14	13
Angle	-	-	9
El. Quality	0.83	0.11	-



(a) Aspect ratio

(b) Skewness

(c) Element quality

Figure 5: Global element distribution concerning aspect ratio, skewness and elemental quality.

### 4.3 Newton-Raphson algorithm

Newton-Raphson algorithm [14] assumes a linear connection between the Piola-Kirchhoff second stress tensor and Green's displacements, and was used to obtain convergence by dividing the external force (in this case applied pressure from the inflatable plate) in a set number of sub-steps, and for every sub-step iterate for equilibrium for the sum of internal forces, being the sum of all elemental forces. Internal forces are calculated individually for each element using a tangential stiffness matrix. The difference of the sum of all internal forces and the external forces are compared to a given tolerance value, and displacements are incrementally adjusted for calculating a new tangential stiffness matrix if this condition is not satisfied. After a successful iteration, an extra incremental load is applied until all sub-steps have converged.

### 4.4 Penalty formulation

Penalty formulation is used to avoid large penetrations of bodies. By adding springs with zero stiffness between the nodal points of each contact surface, and adding stiffness in an iterative scheme when the springs have negative lengths, the penetration can get reduced to a very small amount.

The Augmented Lagrange penalty formulation is used for all contacts in this report, due to its simple setup, compatibility with all contact types and because it results in relatively low penetrations. It is formulated as

$$p = k_p x_p + \lambda \quad (37)$$

Where  $k_n$  is the spring stiffness,  $x_p$  is the penetration and  $\lambda$  is an additional term that differentiates the Augmented Lagrange formulation from pure penalty. The penetration  $x_p$  is compared to a tolerance in each Newton-Raphson iteration. If penetration is bigger than a given tolerance, the Augmented Lagrange formulation increases the value of  $\lambda$  until the condition is fulfilled, without updating the spring stiffness (as in pure penalty). This results in smaller penetrations and a few more iterations. For example,

$$p = k_p x_p + \lambda \rightarrow 10 = 1000 \cdot x_p + 0 \rightarrow x_p = 0.01 > \epsilon_p$$

Updating the additional term results in smaller penetration without updating the spring stiffness [ $\lambda = 0 \rightarrow \lambda = 5$ ] which gives

$$p = k_p x_p + \lambda \rightarrow 10 = 1000 \cdot x_p + 5 \rightarrow x_p = 0.005 < \epsilon_p$$

In this case, the use of Augmented Lagrange resulted in a penetration of 0.005 instead of pure penalty (where  $\lambda = 0$ ) with a penetration of 0.010. The Augmented Lagrange also holds the benefit of being used at any type of contact.

For all contacts, the penetration tolerance was chosen as one tenth of the element size in contact and the pinball radius (volume for contact search size) was chosen as one half of the elemental size.

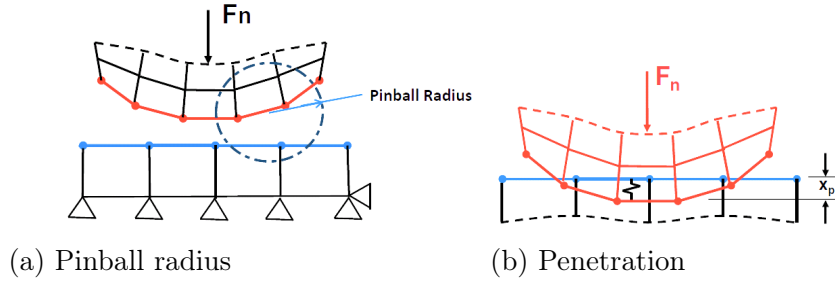


Figure 6: Illustration of pinball radius and penalty formulation. Pinball radius on figure (a) show the contact search size, and figure (b) show penetration distance denoted  $x_p$ , and normal force denoted  $F_n$ .

### 4.5 Detection points

Augmented Lagrange uses integration point detection, which results in more detection points (compared to nodal points), since there are more points to be analyzed for penetration. Gauss integration points were used. Contact behavior is chosen as symmetric for all contact, to simply avoid extra penetration at the cost of extra computing time.

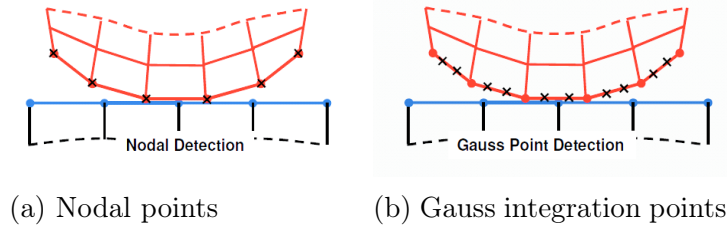


Figure 7: Detection points used for the penalty function.

### 4.6 Weak Springs

To avoid rigid body motion and for easier convergence, weak springs were added. The stiffness of the springs were chosen to have as small resulting reaction force as possible, while the system still being able to converge. How force reaction depend on spring stiffness is shown in the figure below. The figure shows spring stiffness correlation with its reaction forces for a coarse mesh. For a refined mesh, the reaction forces got larger. A 5 N/mm spring stiffness with the mesh shown in table (7) generated a reaction force of 60 N, which is negligible to the external forces of 20 tonnes (196 kN).

### 4.7 Time increment

For transient thermal analysis, an incremental time step has to be chosen, according to

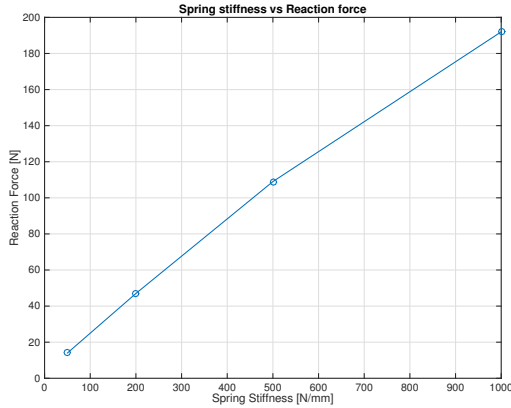


Figure 8: Weak springs [N/mm] vs. force reaction of the global system. Smaller spring stiffness results in smaller reaction forces.

$$\Delta t \leq \frac{length_e^2}{k/\rho c} \quad (38)$$

Where  $length_e$  is the length of an element,  $k$  is the thermal conductivity,  $c$  is the materials speed of sound and  $\rho$  is the material density. The time increments results in 3ms.

## 4.8 Fatigue

Fatigue analysis were made using the RCC-MRx standard [13], a standard commonly used in e.g. nuclear environments. Fatigue analysis was made in regions of interest where fatigue failure were most likely to occur. Membrane stress, bending stresses and peak stresses are obtained by adding a *linearized stress intensity* to several defined paths (straight lines between two points i space) in regions of interest, and the maximum range is used for analysis. Discrete points are distributed along a defined path, where stress values are given to each point by an interpolated value of its elemental nodal values. Each point is given a specific value for its peak stress, membrane stress, bending stress and total stress which are key parameters in using the RCC-MRx standard.

The RCC-MRx does not involve material data for the material used in this project, and can therefore not be officially valid as RCC-MRx approved. Material data used in this analysis will be for different materials in a wide range of harder and softer materials, creating a significant validation that the product will hold for the fatigue limit.

## 4.9 Boundary Conditions Transient Thermal

Heat flow from convection was modeled using only specific heat and thermal conductance and their dependence on temperature. In areas where heat flow between parts

was expected, contact was defined as bonded. The end plate of the CCR had a static boundary surface temperature of 4K, and all other bodies were initially defined with a temperature of 295.15K, causing heat flow to occur through temperature difference.

Also radiation was modeled using a spherical layered shell around the DAC and CCR with a static temperature of 295.15K, and an emissivity of 0.1.

To fully capture the entire structure of the DAC and CCR, half symmetry was used, which was cut between the two diffraction windows, see figure (1c)

## 4.10 Boundary Conditions Static Structural

Frictionless contact were applied on all contact except for threaded (threaded lid/base part and all screws) and glued parts (diamonds/seats) which were modeled using bonded contact. Frictionless contact uses unilateral contact, which is a non-linear contact that allows for separation, and a zero coefficient of friction. Bonded contact is a linear contact type that does not allow sliding between faces or edges. The symmetry planes and the area for convection contact between the CCR and the DAC are also modeled with frictionless contact.

# 5 Results

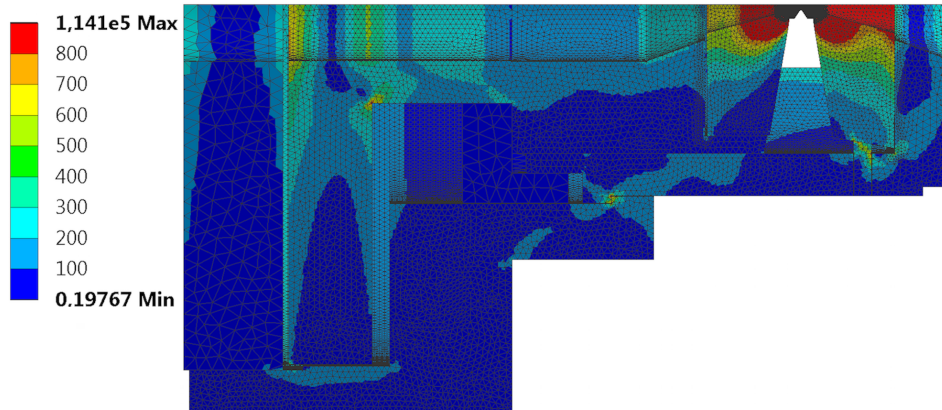
## 5.1 Structural Analysis of Initial Design

Results are given by figures below. Legends represents stresses in megapascals [MPa]. Maximum allowable stress in regions containing copper-beryllium is set to 800 MPa, to avoid plasticity with a safety factor of 1.2. Red rectangles in figure (9b) indicate areas exceeding yield criteria. These regions are modified in the following sections to fulfill the criteria.

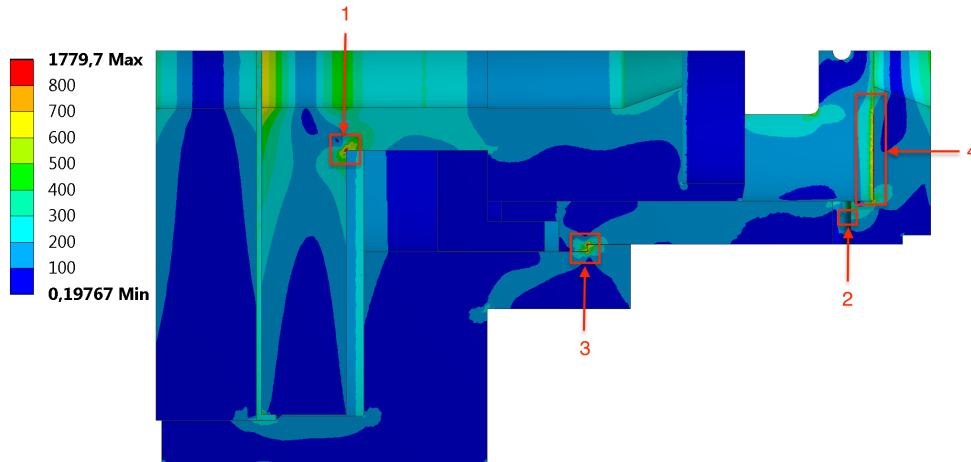
## 5.2 Submodels of Structural Analysis

Rectangle 2 in figure (9b) displays stresses above the yield criteria for the connection between a screw and the diffraction aperture. Defining a smaller sub model with imported displacements from the global model applied on cut boundaries, but with a much denser mesh, local high stress concentration could be examined. Peak stresses were found on a few nodal intersections, on the boundary of the symmetry conditions. The peak stresses were limited to a small area, covering less than one element. Local peak stresses shown in figure (10b), mesh independent behavior shown in figure (10c), the strong gradients and lack of physical explanation for the behavior show signs of a numerical singularity being the most probable explanation.





(a) Stress distribution and element configuration.



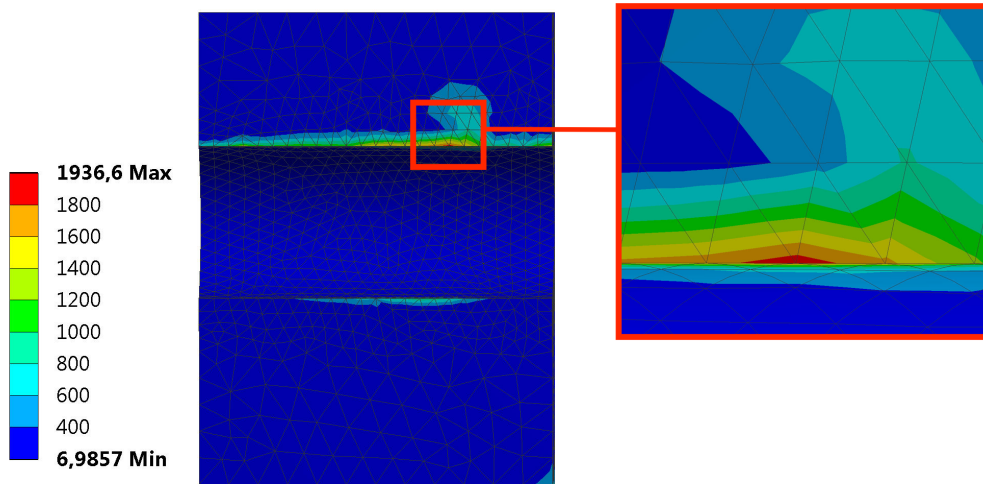
(b) Global stress distribution of initial design, solely displaying parts with copper alloy C17200 AT(TF00). Red rectangles indicate areas exceeding yield criteria.

Figure 9: Global stress distribution of initial design. Figure (a) display stress distribution within seats, diamonds and elemental configuration. Figure (b) display interesting areas for modifications. Legend displays stress values in [MPa].

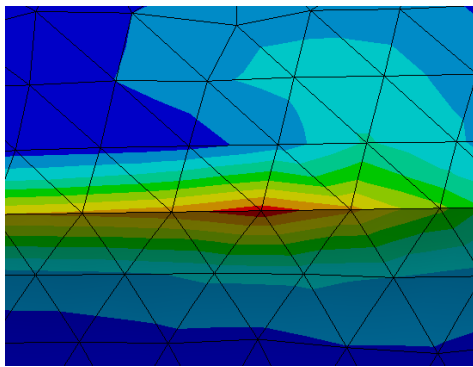
## 5.3 Deciding Dimensions to Avoid Yield

### 5.3.1 Bottom plate radius

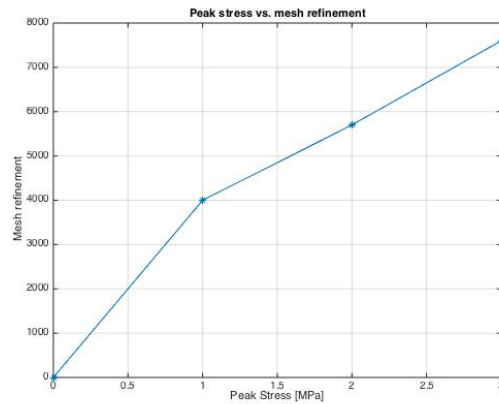
The 4th red rectangle in figure 9 was investigated, and a combination of two parameter decreased the stresses to an acceptable level: a fillet radius and a thickening of the lower plate. Through an iterative scheme, a fillet radius of 2.5 mm was chosen.



(a) Submodel of screw holes with stresses shown in MPa. At the nodal intersection of six elements a peak stress is evaluated.



(b) Singularity viewed from below to show nodal connection where singularity occurs.

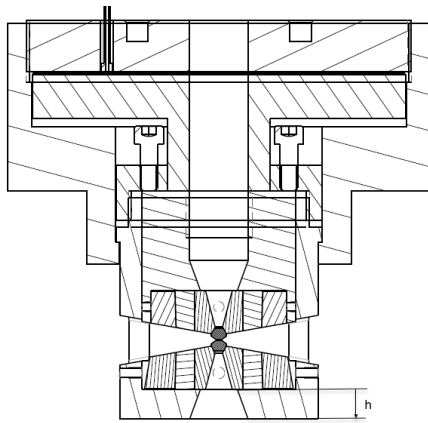


(c) Peak stresses plotted against mesh refinement or edges around screw holes.

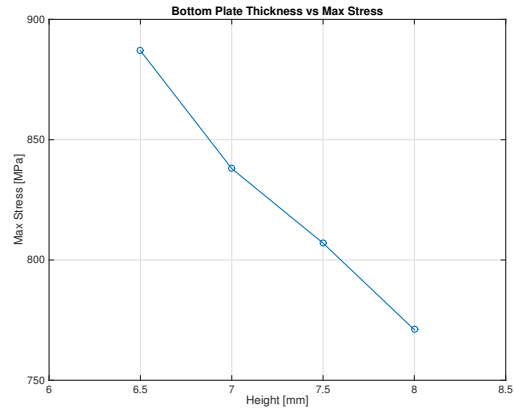
Figure 10: Closer look at high stress area (rectangle 2 in figure 9). Figure (b) show singularity shown from below to illustrate nodal connection of elements, and (c) show peak stresses plotted against mesh refinement around edges of screw hole. Legend displays stress values in [MPa].

### 5.3.2 Thickness of Part 1 Lower Plate

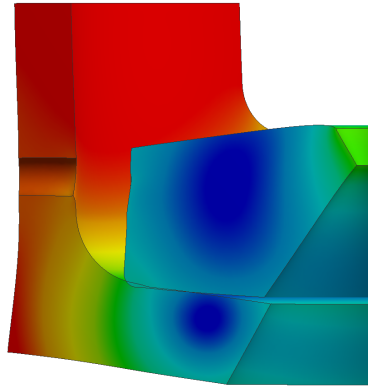
The second step in decreasing the stresses in rectangle four was to add an additional thickness to the bottom layer, as can be seen in figure 11.



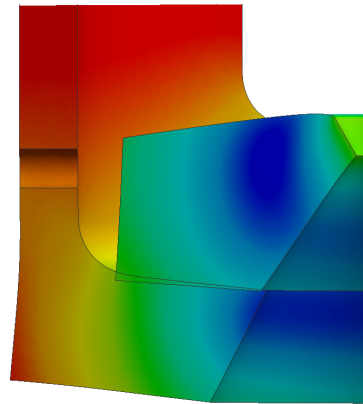
(a) Thickness  $h$



(b) Thickness vs. max stress in part



(c) Exaggerated deformations with initial thickness.



(d) Exaggerated deformations with added thickness.

Figure 11: Added thickness and its correlation to maximum stresses of part. With criterion stated earlier, a max stress of 800 MPa is allowed for all parts of BeCu, meaning a minimum thickness of lower part is somewhere around 7.5 mm. With added material, buckling is avoided, and the steel seat is in contact with a larger surface BeCu.

### 5.3.3 Filet Radius on Piston

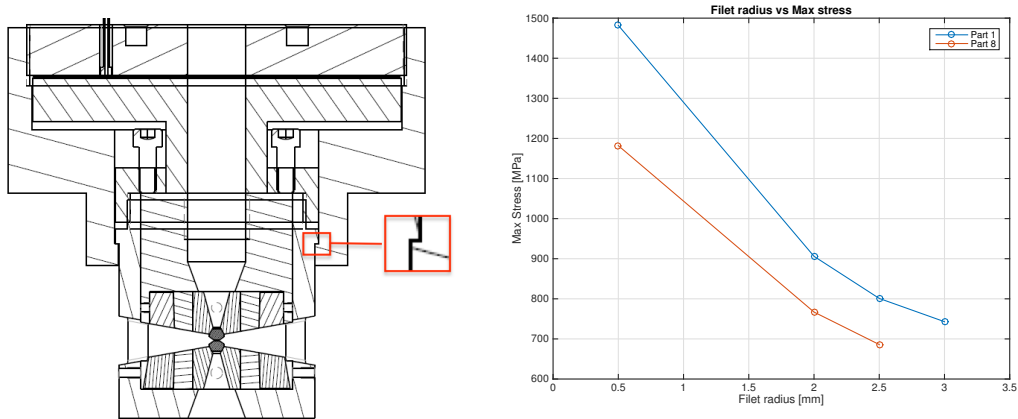
To avoid high stress concentrations on the piston (see rectangle 1 in figure (9b)), a 5 mm filet radius was added, which decreased the maximum stress to 495 MPa, which is within the stress criteria, see figure (14).

### 5.3.4 Width of diffraction window

The diffraction aperture was increased with a total of 20°, which was the maximum allowable increase before the maximum allowable stress was reached.

### 5.3.5 Filet Radii around Lip Surface

The 3rd rectangle in figure (9b) was investigated by increasing the lip filet radius in an iterative scheme, and investigating different filet radii for each part. The results are shown in figure 12.



(a) Lip surface, initially with sharp corners. (b) Added filet radius of each part and the corresponding max stress of the part

Figure 12: The lip surface was initially increased from 1 mm to 6 mm and a variety of radii for each part and was investigated with the 800 MPa-criterion to avoid yield stress with a safety factor of 1.2.

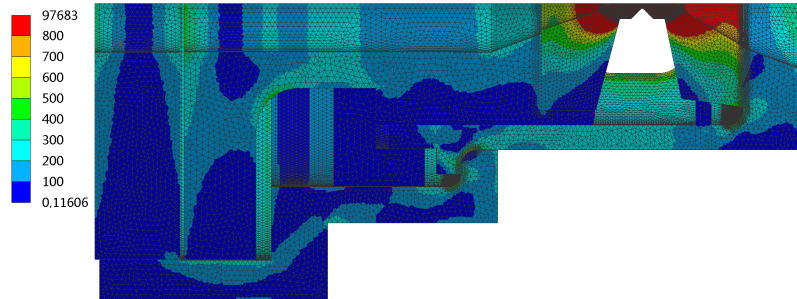
### 5.3.6 Global Radius

Using a European standard instead of an American standard which the original model was designed after, the maximum allowable pressure is 200 bars (compared to the American standard that allows  $2000\text{psi} \approx 138\text{bar}$ ) which in turn allows the diameter of the piston and threaded lid to be decreased to 84 mm (compared to 102 mm) while still generating the same force. By decreasing the volume, there is less mass to cool down - resulting in lower cooling time.

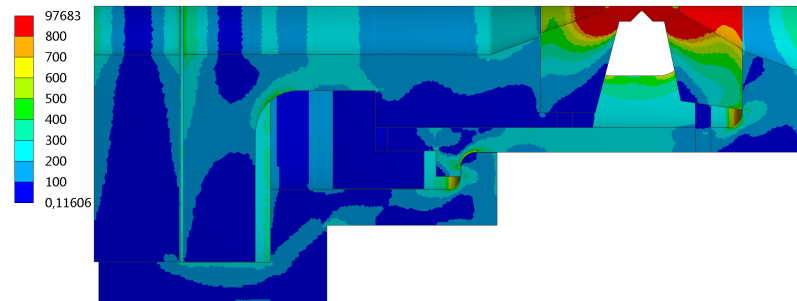
## 5.4 Results from improved design

### 5.4.1 Stresses global geometry

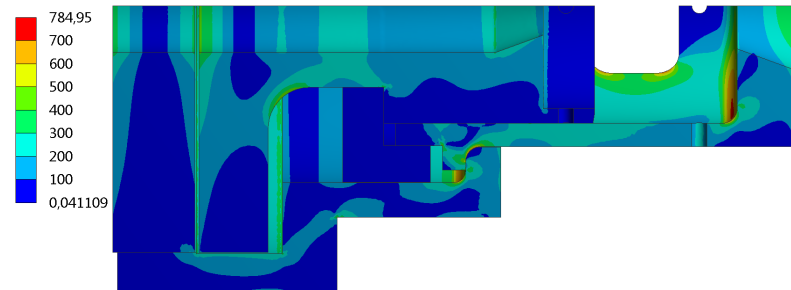
The figure below show stresses on the modified design, re-constructed according to previous mentioned alterations.



(a) Global stress distribution with displayed mesh.



(b) Global stress distribution without displayed mesh

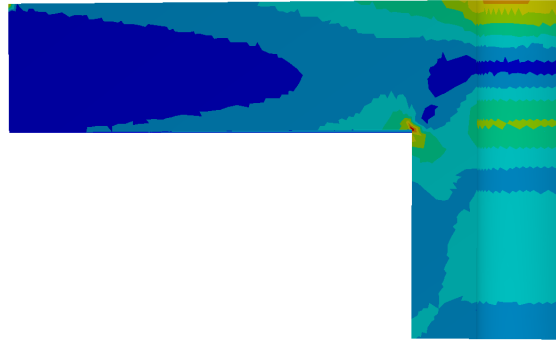


(c) Global stress distribution of parts made from Copper Beryllium.

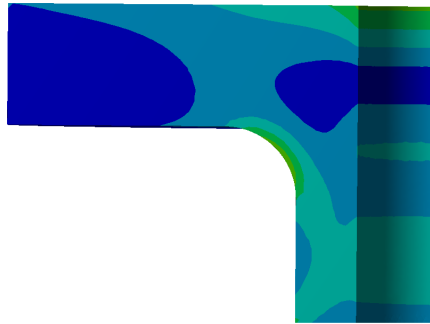
Figure 13: Cut section of DAC displaying stress distribution. Legend displays stress values in [MPa].

### 5.4.2 Stresses Modified Piston

The overall radius was significantly decreased, and a  $5\text{mm}$  fillet radius was added. The resulting stress distribution was according to the figure below.



(a) Stress distribution initial piston.

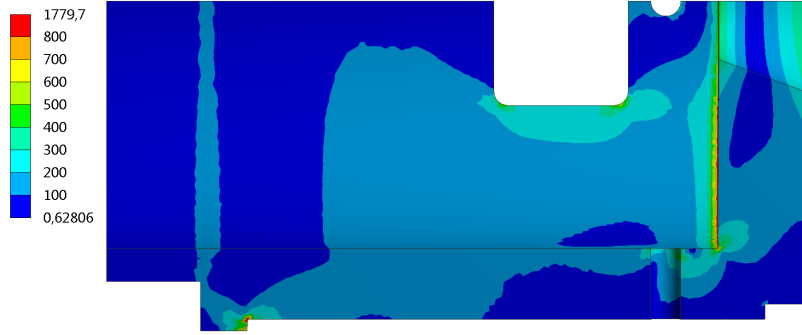


(b) Stress distribution of modified piston.

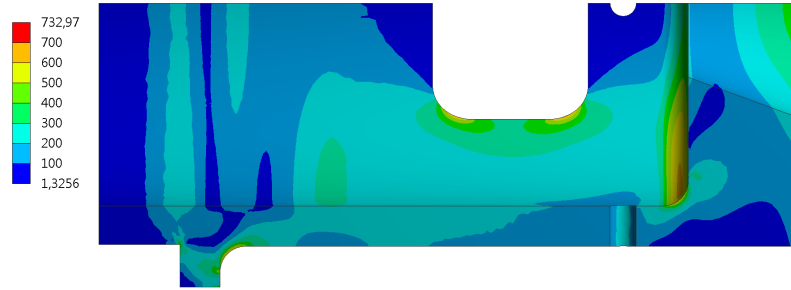
Figure 14: Quarter symmetry of piston displaying stress distribution. Red colors show areas exceeding yield criterion. The initial design of the piston had stresses beyond yield criterion, and the modified version had stresses within yield criterion (maximum stresses of modified piston:  $496\text{ MPa}$ ).

### 5.4.3 Stresses Modified Diffraction Aperture

Diffraction aperture before and after modifications are shown in the figure below. The initial design had stresses exceeding yield criterion and the modified design has stresses all within yield criterion.



(a) Stress distribution initial design of part 1.



(b) Stress distribution of modified design of part 1.

Figure 15: Quarter symmetry of piston displaying stress distribution. The initial design had stresses beyond yield criterion on several places, and the modified version had stresses all within yield criterion. Legend shows stresses in [MPa]

#### 5.4.4 Fatigue

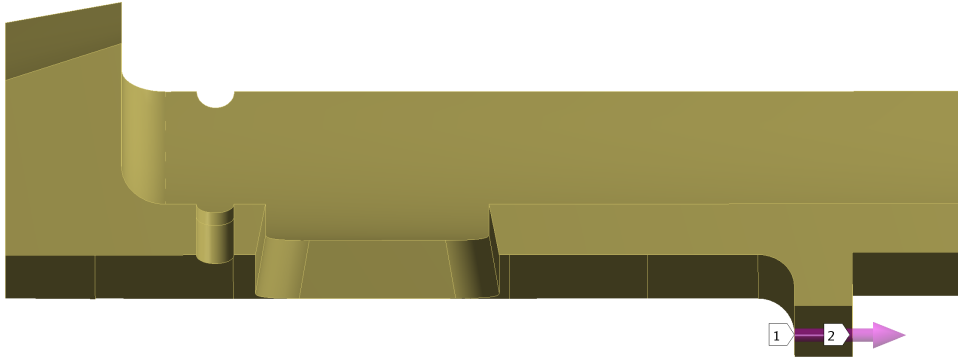
$\bar{\epsilon}_3$  is given by [eq. 33], which is increasing for greater values of  $K_\epsilon$ . The maximum value of  $K_\epsilon$  is given by the standard (by investigation of *all* materials) to the maximum value of  $K_\epsilon = 2.02$  (for non-alloy steel A3.11NAS which is assumed to be of greater value than a corresponding value for C17200 AT(TF00)). The same can be done with  $K_\nu$  reaching a top value at  $K_\nu = 1.36$  (for steel A3.3S). These approximations will probably result in larger total strain, resulting in shorter life times compared to the real value. If this fatigue analysis holds for the larger value, it would also hold for the real value.

$$\begin{aligned} \overline{\Delta\epsilon_1} + \overline{\Delta\epsilon_2} + \overline{\Delta\epsilon_3} + \overline{\Delta\epsilon_4} &= \\ &= \frac{2}{3E}(1 + \nu)\overline{\Delta\sigma_{tot}} + \frac{2(1 + \nu)}{3E} \frac{\Delta\sigma_t}{100} \left(\frac{\Delta\sigma_t}{K}\right)^{1/m} + (K_\epsilon - 1)\overline{\Delta\epsilon_1} + (K_\nu - 1)\overline{\Delta\epsilon_1} \end{aligned}$$

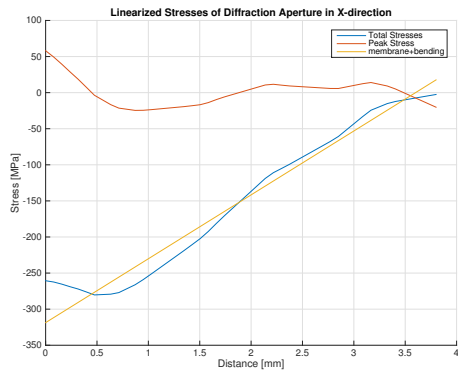
With values from linearized stress output from Ansys:  $\overline{\Delta\sigma_{tot}} = 257MPa$  and  $\Delta\sigma_t = 122MPa$ , and  $m = 0.351$  and  $K = 711.9$  from the standard, the total strain results in  $\epsilon_{imaginary} = 0.004$  which according to the graphs [RCC-MRx A3.47] hold for infinite life.

One must emphasize that this is just an indicator of infinite life, and not a guarantee, since the RCC-MRx is only valid for strictly following the standard with the available material data.

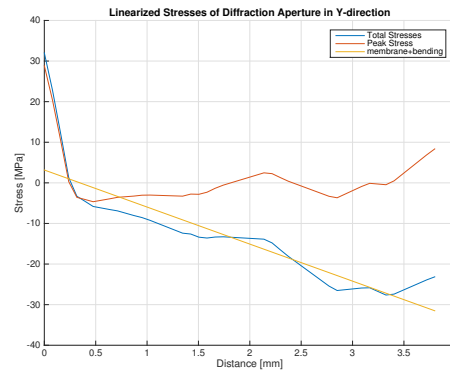




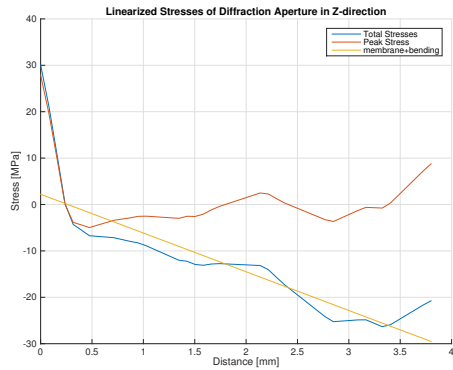
(a) Path between two points in the diffraction aperture.



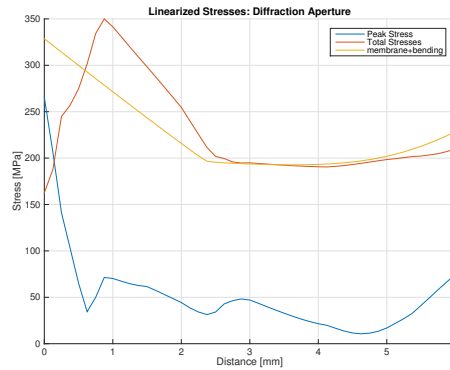
(b) Linearized stresses in x-direction.



(c) Linearized stresses in y-direction.



(d) Linearized stresses in z-direction.

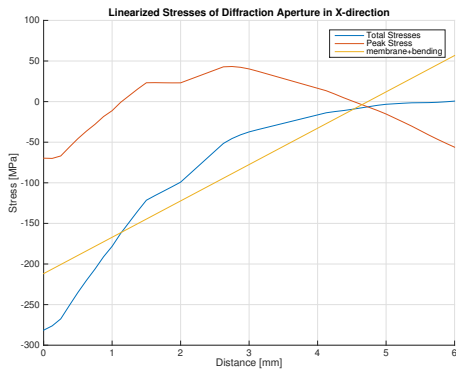


(e) Total linearized stress intensities.

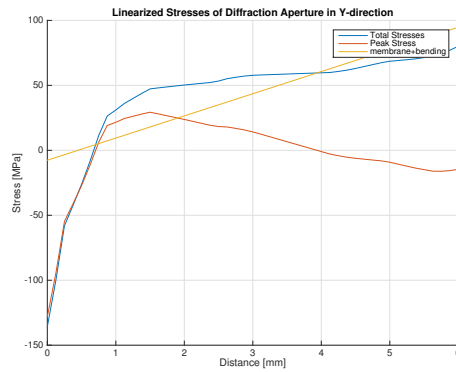
Figure 16: Linearized stresses along a defined path (see *figure a*) in the diffraction aperture, used for fatigue analysis. Legend displays peak stresses (red), membrane and bending stresses (yellow) and total stresses (blue).



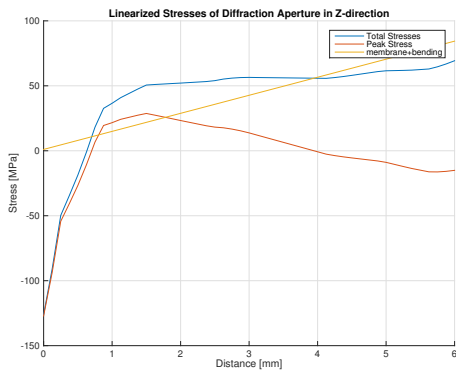
(a) Path between two points in the base part.



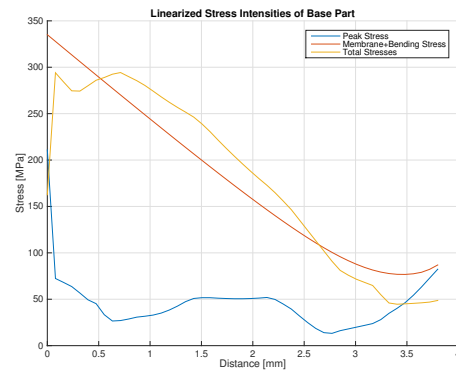
(b) Linearized stresses in x-direction.



(c) Linearized stresses in y-direction.



(d) Linearized stresses in z-direction.



(e) Total linearized stress intensities.

Figure 17: Linearized stresses along a defined path (see *figure a*) in the base part, used for fatigue analysis. Legend displays peak stresses (red), membrane and bending stresses (yellow) and total stresses (blue).

## 5.5 Thermal Analysis

### 5.5.1 Thermal Analysis of Initial Design

The results of the time-dependent thermal cooling of the initial design can be shown in figure 18.

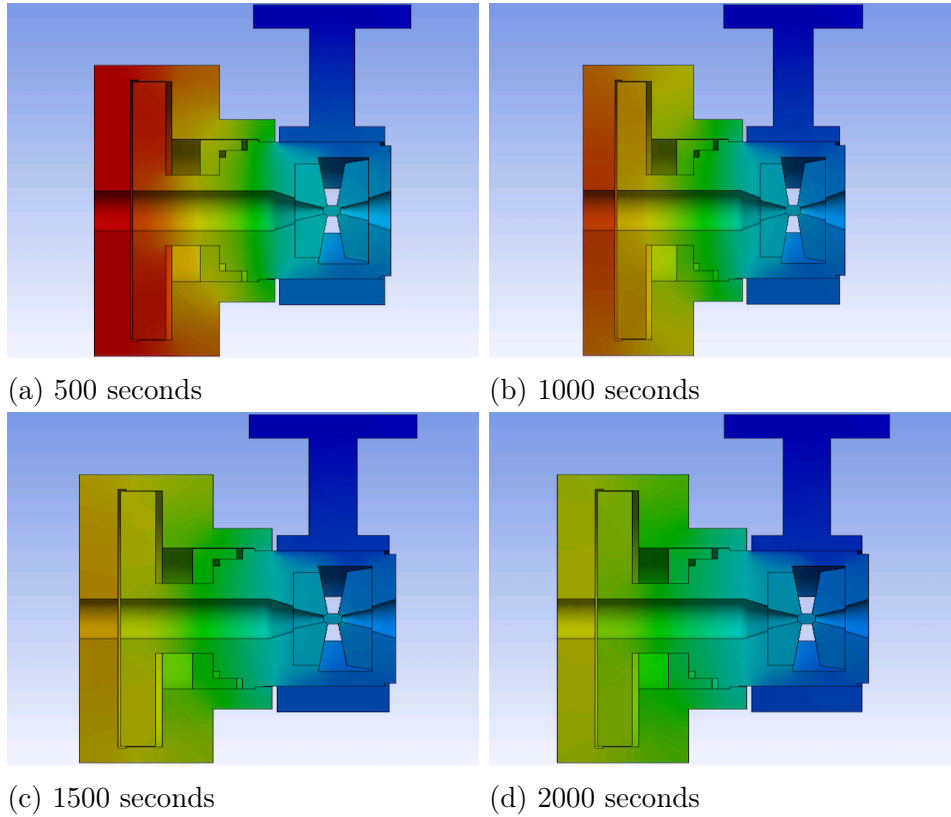


Figure 18: Temperature distribution in intervals of 500 seconds for the initial design. Images displaying half symmetry of DAC with CCR. Dark blue color represents 4K, and red represents 295.15K.

### 5.5.2 Thermal Analysis of Modified Design

The results of the time-dependent thermal cooling of the modified design can be shown in figure 19.

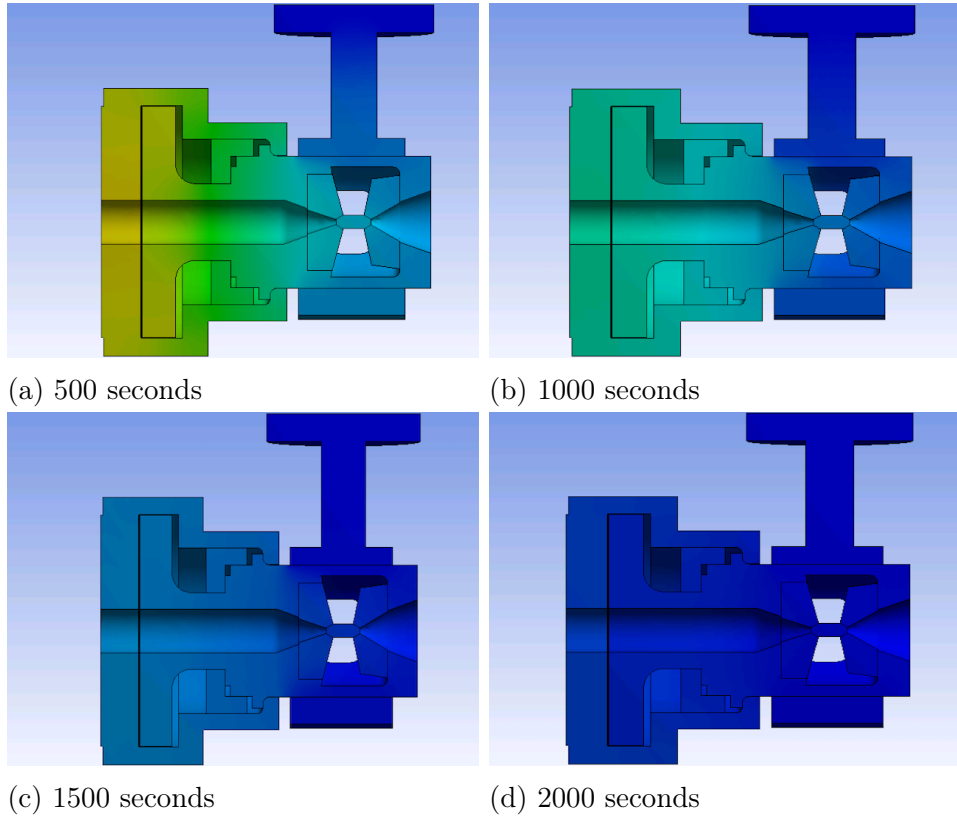


Figure 19: Temperature distribution in intervals of 500 seconds for the modified, improved design. Images displaying half symmetry of DAC with CCR. Dark blue color represents 4K, and red represents 295.15K.

Table 9: Discrete temperature values for diamonds in initial and modified design over time.

Time (s)	Initial (K)	Modified (K)
0	295.15	295.15
500	53.5	46.5
1000	42	25
1500	37	11
2000	33	5.6
3000	26	-
4000	21	-
5000	16	-
6000	11	-
7000	7.2	-
8000	7.0	-

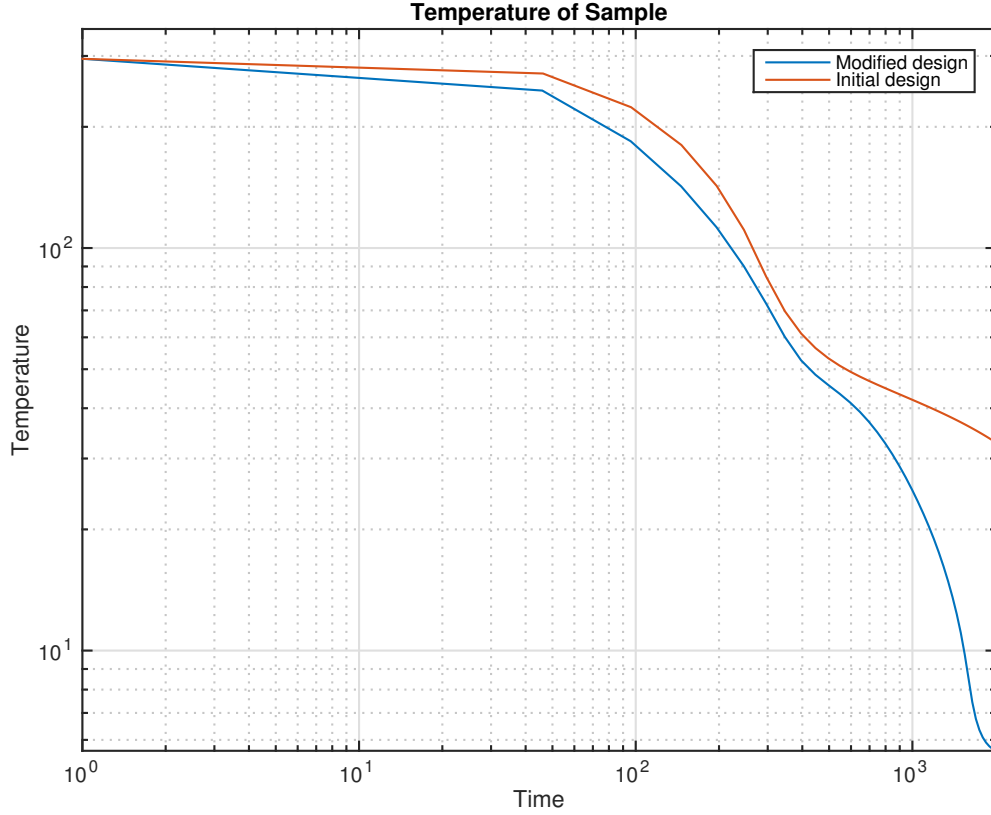
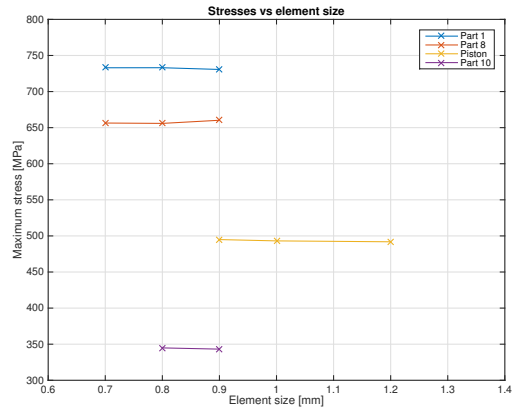


Figure 20: Temperatures time-dependency for diamonds in initial- and modified design.

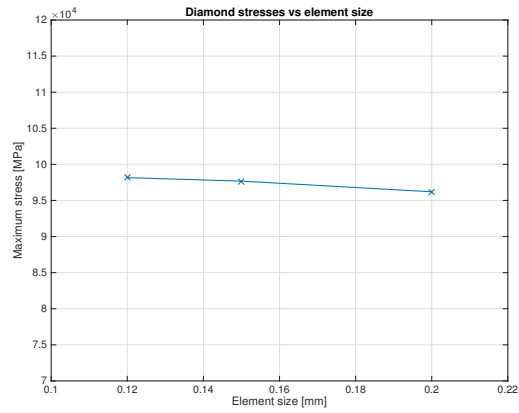
## 6 Validation

### 6.1 Validating Mesh

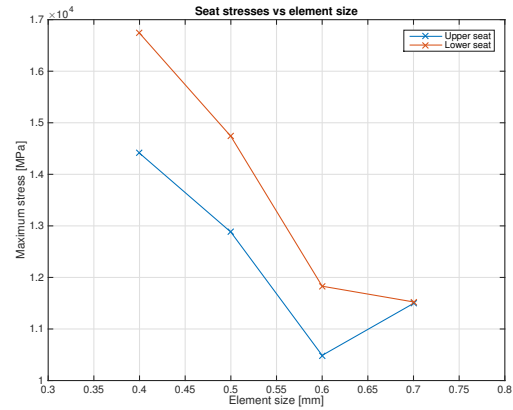
Mesh refinement to each part is shown in the figure below. The seats seem to be completely mesh-independent. If one were to look closer, the plotted curve of figure (d) is only plotting the maximum stresses. The seats seem to have a singularity at one of its edges. When adding a rounded of corner, the peak stress is changing location, which is an indication of a numerical singularity. Another indication of numerical error is the extreme gradients on these elements, with high stresses spreading across less than half an element. In reality, these seats are known to function and not much consideration is needed. These areas are known to yield with the first use, causing the structure to harden plastically, something this FEA-analysis will not allow since its modeled only within the elastic regime. One could implement a non-linear material model to fully capture this behaviour, something that was considered not necessary.



(a) Part 1 and part 8.



(b) Part 7 and part 4.



(c) Seats

Figure 21: Mesh refinement and corresponding maximum stresses for each part. Figure (d) is referring to part 2 and 3.

## 6.2 Extra Validations

When analyzing contact areas, the reaction forces of each contact pair is fairly close to the 24kN which is the quarter symmetry equivalent of 10 tonnes applied force added, which is an indication of good results.

Table 10: Reaction forces for contact surfaces (given notation contact/target), and its difference to reference value in percent.

Contact Bodies	Contact / Target [N]	$\Delta\%$
Spacer/Seat	24414 / -24414	0.4
Seat/Diamond	24399 / -24399	0.4
Diamond/Seat	24391 / -24391	0.5
Seat/Diffraction Aperture	24408 / -24408	0.4
Diffraction Aperture/Base Part	24392 / -24386	0.5
Reference	24515 / -24515	0

Also, the stresses are distributed continuously throughout the model. Stress distribution and stress peaks has changed according to changes made in the iterative process, which makes sense.

The reaction forces of the weak spring added to avoid rigid body movement are 60N (of 2x10tonnes) which is a negligible amount.

## 7 Discussion

The transient thermal analysis of the initial model (made with inconel 718) was an analysis made to relatively compare the modified version. This test has already been made in a real life experiment, a process which took about 8 hours to complete. In the FEA-analysis, there seems to be a significantly faster cooling (around 2.5 hours to reach 7K). This is partly due to the CCR being 4K from the start in the analysis, where it in reality needs time to cool down, which affects the overall cooling time. Also, the values for emissivity is roughly approximated which greatly affects the results. The model is using only thermal conductivity, specific heat and heat radiation, and not taking surface roughness into account. Also, as can be seen in *Section 2* thermal properties are estimated to values of nickel instead of Inconel and an un-treated Copper-Beryllium opposed to heat treated and precipitation hardened. These factors combined causes the analysis to cool down much faster than real life experiments. On the other hand, the aim of the project was not to reach a goal of an exact time, but just to make the cooling as fast as possible. Therefore, the relative difference between the analysis can show the benefits of re-designing the model and indicate roughly the beneficial time.

In real life, one could consider the possibility of putting the entire product in a "pre-cooling" phase, which could be a liquid nitrogen bath which would cool the entire DAC to 80K almost instantaneously. On the other hand, one could argue that such fast cooling could cause thermal stresses. In that case, it would be beneficial to do a combined transient thermal and structural analysis, instead of two separate ones.

This report has shown that just modifying the DAC the total cooling time can be decreased by a significant amount. By adjusting the CCR, the time could be decreased even more. One could for instance expand the convection area to cover not only the diffraction aperture but also the base part, thus increasing the convection area by more than 100%. This could easily be done by surrounding the base part with copper-bands connected by strings to the CCR.

Also, for the connection between the CCR made with Copper and the DAC made with Copper-Beryllium, there will be a difference in thermal expansion coefficients, affecting the contact heat surface. By using a screw, a nut and a spring on the back side of the CCR, the contact surface will remain automatically during temperature changes.

Fatigue analysis was made using the RCC-MRx method, which is a standard used in nuclear environments and also for ESS equipment. The standard uses specific material parameters, some of which could not be gathered without the standard. Because this specific material does not exist within the standard, values were approximated using other sources where possible. When other material parameters could not be gathered elsewhere, the total spectra of material parameters (for both softer and



harder materials), which indicated infinite life. One must emphasize that this is not a guarantee approved by the RCC-MRx, but rather a good indication.

One could *also* argue that fatigue failure analysis is not relevant for materials within the elastic regime, since no ratcheting is occurring (especially for 500 cycles). This results in two strong arguments for the fatigue requirements being met.

As can be seen in the figure [17c], mesh refinement does not really say much about the seats. With a closer look at the actual stress distribution, one can see clear signs of singularities at the edges of these seats. Evidence of being a numerical singularity is strong gradients and no signs of reaching a stress limit when refining the mesh. Another contributing factor may be the material model used for these parts which is linear, although in reality deformations are known to be plastic.

Diamonds, approximated from highly anisotropic to isotropic mechanical properties, and steel Vascomax c350 (used for seats), are not as thoroughly simulated as parts made out of copper-beryllium. This is mainly because these parts are known to function with the given dimensions, and simulations are therefore not necessary. One improvement to be made in future simulations is to simulate the seats with non-linear simulations to fully capture the initial plasticity occurring in these parts. One could also try to optimize the diamonds with simulations, which would be rather more difficult.

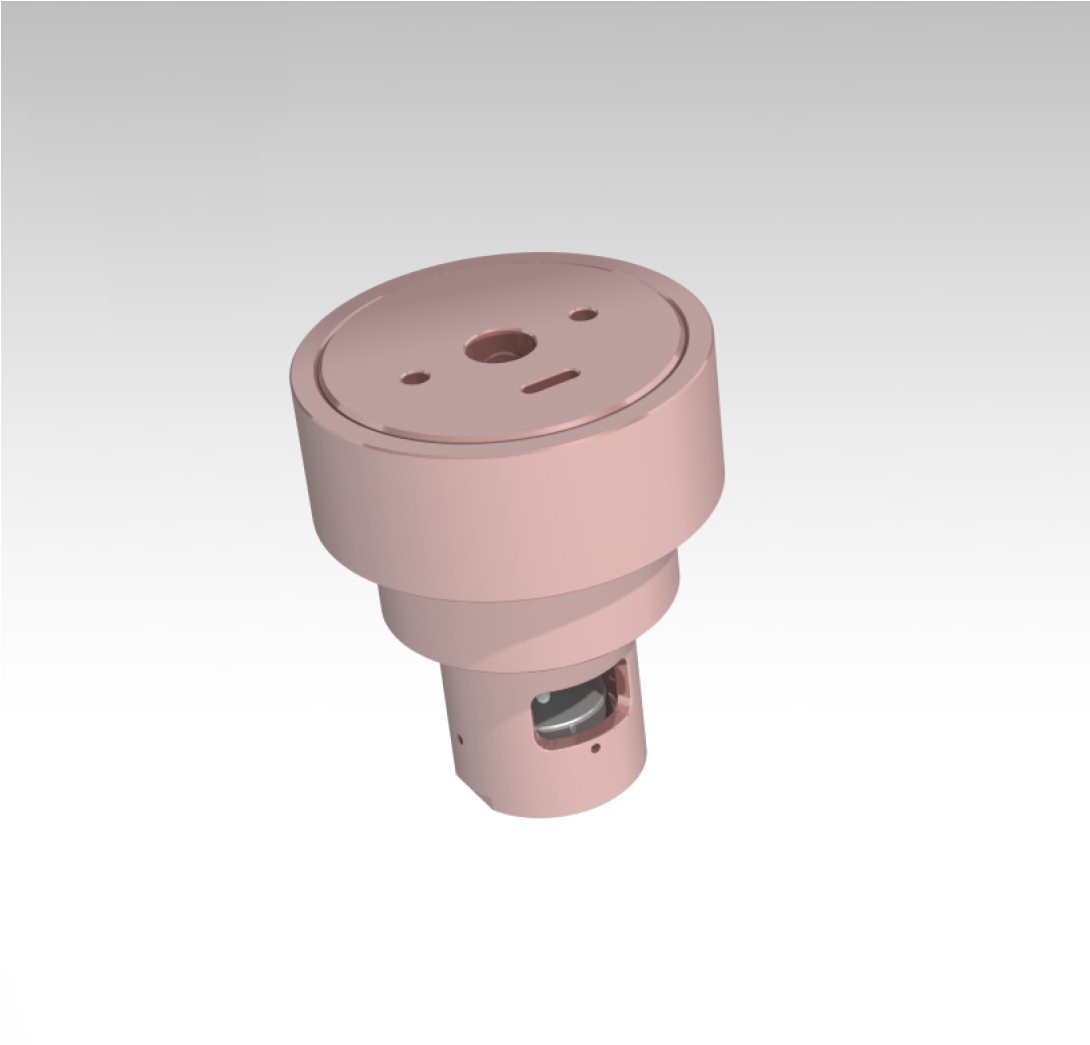


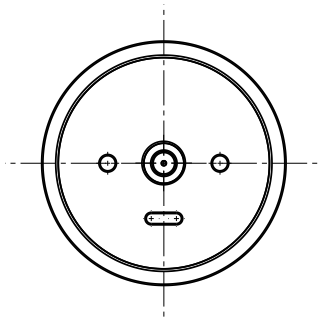
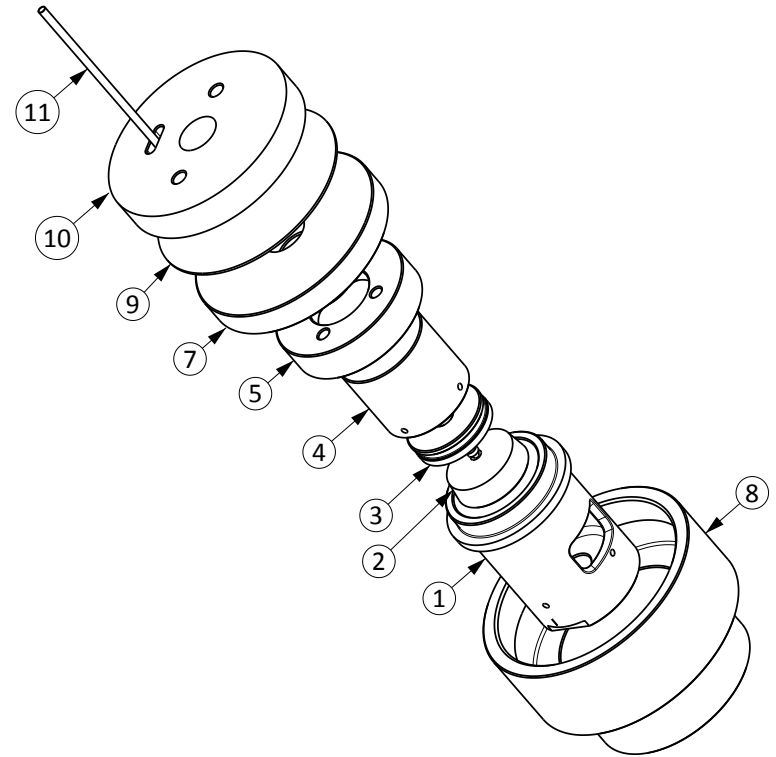
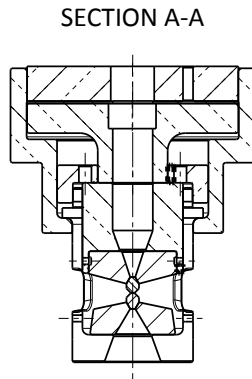
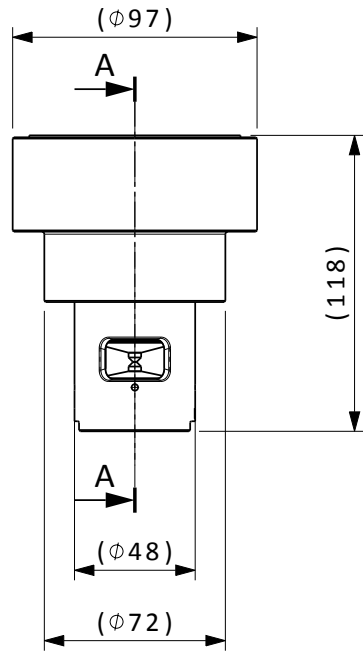
Figure 22: Rendered image of the finished product.

## References


- [1] C.J. Ridley, M.K. Jacobsen, K. V. Kamenev, *High pressure neutron and X-ray diffraction at low temperatures* De Gruyter Pages 19, 175, 189 2014.
- [2] C.J. Ridley, K.V. Kamenev, *A finite-element study of sapphire anvils for increased sample volumes*  
2015
- [3] Steven W. Van Sciver, *Helium Cryogenics* Table 2.5, Springer 2012
- [4] R. Michael McClintock, Hugh P. Gibbons, *Mechanical Properties of Structural Materials at Low Temperatures* p.22 U.S. Department of Commerce National Bureau of Standards Monograph 13 1960
- [5] Robert J. Corruccini, John J. Gniewek, *Specific Heats and Enthalpies of Technical Solids at Low Temperatures* Table 4, U.S. Department of Commerce National Bureau of Standards Monograph 21 1960
- [6] Joseph R. Davis, et al., *ASM Handbook* Volume 2, Tenth Edition 2011
- [7] R.W.Powell, C.Y. Ho, P.E. Liley, *Thermal Conductivity of Selected Materials* P.22 National Standard Reference Data System, NBS 8 1966
- [8] E.D. Marquardt, J.P. Le, Ray Radebaugh, *Cryogenic Material Properties Database* page 2-3, National Institute of Standards and Technology, 2000
- [9] Richards, Brick, *Low Temperature Properties of Normal Beryllium Copper* Table 5 Trans. Amer. Inst. Min. Met. Eng. vol. 200, Pt. 5, 1954
- [10] M. I. Eremets, *High Pressure Experimental Methods*, Oxford Science Publications 1996
- [11] N. Ottosen, H. Petersson, *Introduction to the Finite Element Method*, p.48-58, p.292-299, Pearson 1992
- [12] Smith High Performance Data Sheet Alloy 25 (C17200)
- [13] *RCC-MRx* Section III Tome 1 RB3000 Design and Appendix 3 Afcen, 2012 edition, 2013
- [14] S. Krenk, *Non-linear Modeling and Analysis of Solids and Structures* Cambridge University Press 2009
- [15] Trans. Amer. Inst. Min. Met. Eng., *Low Temperature Properties of Normal Beryllium Copper* Vol. 200, Pt. 5, pp.574-580 1954

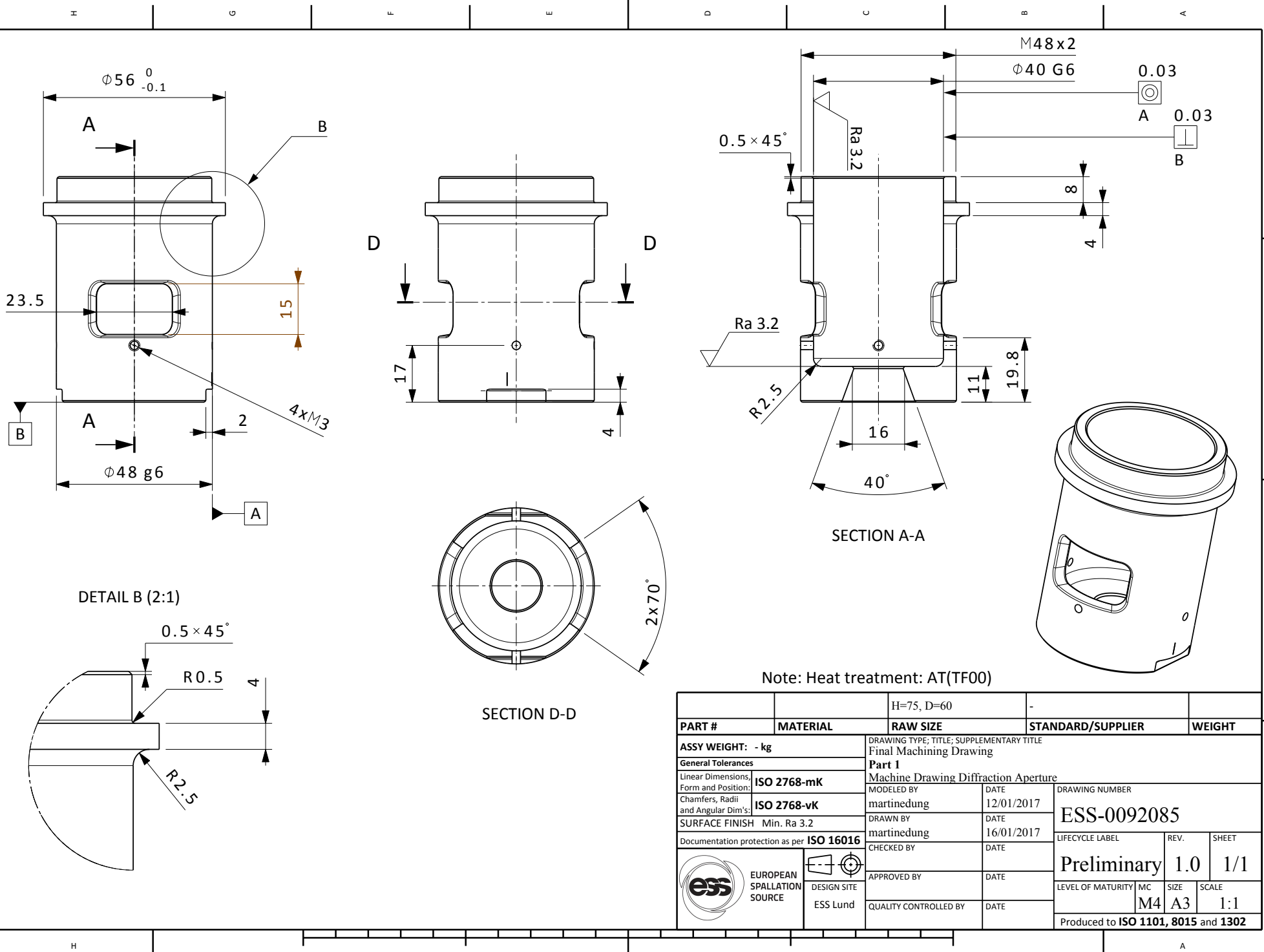
- [16] S.H. Lee, S.W. Kim, K.H. Hang *Effect of Heat Treatment on the Specific Heat Capacity of Nickel-Based Alloys* International Journal of Thermophysics Vol. 27, pp.288-289 2006

## Appendix A Machine Drawings of DAC




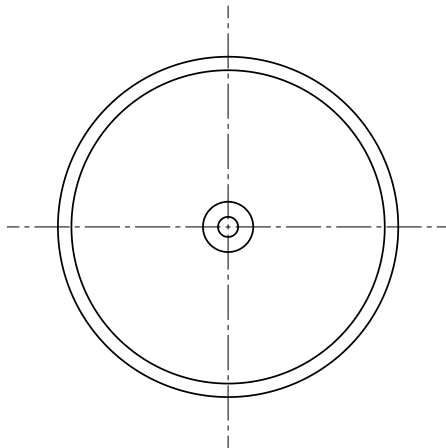
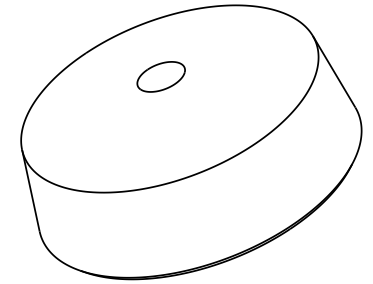
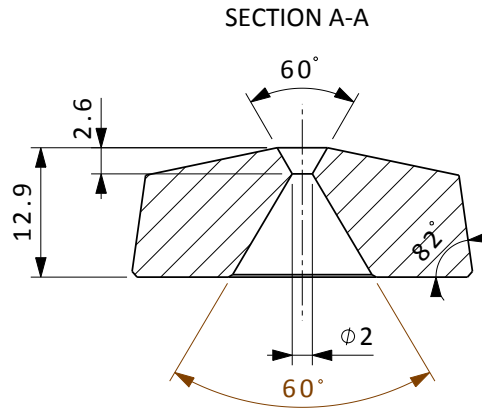
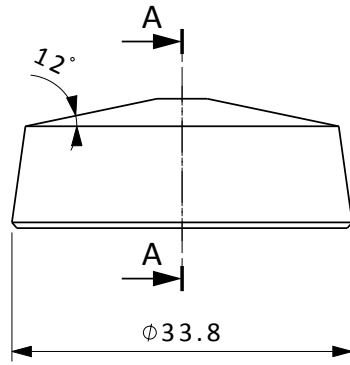
Item	Part Number	Qty	CAD Number	Title	Description	Material	Material std	Material cert.
11	ESS-0092230	1	ESS-0092230	Straw	-	C17200	-	-
10	ESS-0092083	1	ESS-0092083	Threaded Lid	Heat treated AT(TF00)	C17200	-	-
9	ESS-0092229	1	ESS-0092229	Inflatable plate	Heat treated AT(TF00)	C17200	-	-
8	ESS-0091968	1	ESS-0091968	Base Part	Heat treated AT(TF00)	C17200	-	-
7	ESS-0089554	1	ESS-0089554	Piston	Heat treated AT(TF00)	C17200	-	-
5	ESS-0089551	1	ESS-0089551	Screw Holder	Heat treated AT(TF00)	C17200	-	-
4	ESS-0089550	1	ESS-0089550	Spacer	Heat treated AT(TF00)	C17200	-	-
3	ESS-0089549	1	ESS-0089549	Upper Seat	-	Vascomax c350	-	-
2	ESS-0089548	1	ESS-0089548	Lower Seat	-	Vascomax c350	-	-
1	ESS-0089546	1	ESS-0089546	Diffraction Aperture	Heat treated AT(TF00)	C17200	-	-



<b>ASSY WEIGHT: - kg</b>		DRAWING TYPE; TITLE; SUPPLEMENTARY TITLE Assembly Drawing			
<b>General Tolerances</b>		<b>DAC</b>			
Linear Dimensions, Form and Position: <b>ISO 2768-mK</b>		Assembled Drawing			
Chamfers, Radii and Angular Dim's: <b>ISO 2768-vK</b>		MODELED BY martinedung	DATE 21/12/2016	DRAWING NUMBER <b>ESS-0092064</b>	
SURFACE FINISH Min. Ra 3.2		DRAWN BY martinedung	DATE 13/01/2017	LIFECYCLE LABEL <b>Preliminary</b>	
Documentation protection as per <b>ISO 16016</b>		CHECKED BY	DATE	REV. <b>1.0</b>	SHEET <b>1/1</b>
 <b>EUROPEAN SPALLATION SOURCE</b>		DESIGN SITE ESS Lund	APPROVED BY	DATE	LEVEL OF MATURITY MC
			QUALITY CONTROLLED BY	DATE	SIZE M4 A3
					SCALE 1:2
Produced to <b>ISO 1101, 8015 and 1302</b>					



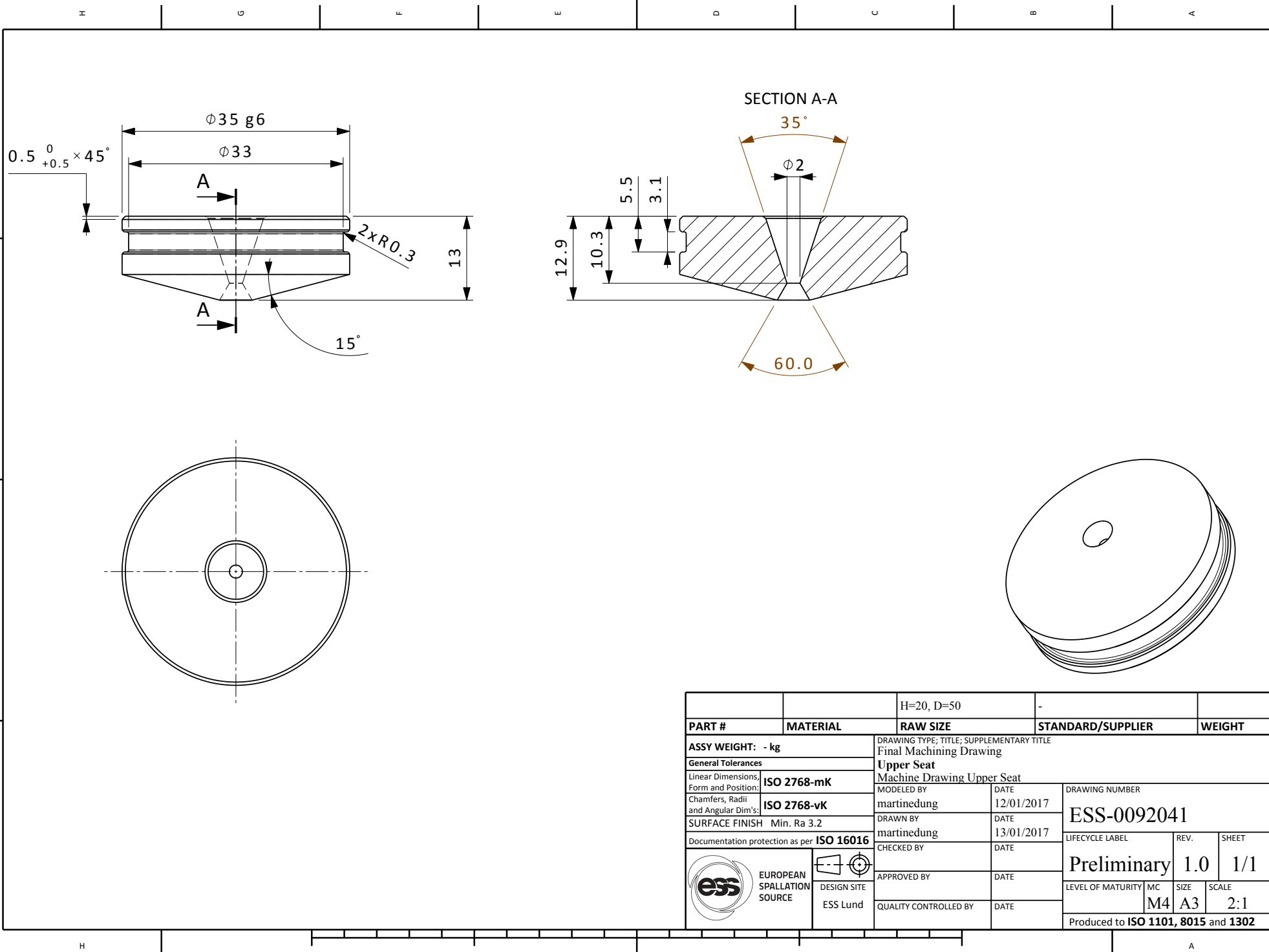
Note: Heat treatment: AT(TF00)

		H=75, D=60		
PART #	MATERIAL	RAW SIZE	STANDARD/SUPPLIER	
<b>ASSY WEIGHT: - kg</b> General Tolerances Linear Dimensions, Form and Position: <b>ISO 2768-mK</b> Chamfers, Radii and Angular Dim's: <b>ISO 2768-vK</b> SURFACE FINISH Min. Ra 3.2 Documentation protection as per <b>ISO 16016</b>		DRAWING TYPE; TITLE; SUPPLEMENTARY TITLE <b>Final Machining Drawing</b> <b>Part 1</b> Machine Drawing Diffraction Aperture		
 EUROPEAN SPALLATION SOURCE DESIGN SITE ESS Lund		MODELED BY martinedung DATE 12/01/2017	DRAWING NUMBER <b>ESS-0092085</b>	
APPROVED BY DATE		DRAWN BY martinedung DATE 16/01/2017	LIFECYCLE LABEL <b>Preliminary</b>	
QUALITY CONTROLLED BY DATE		CHECKED BY DATE	REV. <b>1.0</b>	SHEET <b>1/1</b>
		LEVEL OF MATURITY <b>M4</b>	SIZE <b>A3</b>	SCALE <b>1:1</b>
Produced to <b>ISO 1101, 8015 and 1302</b>				

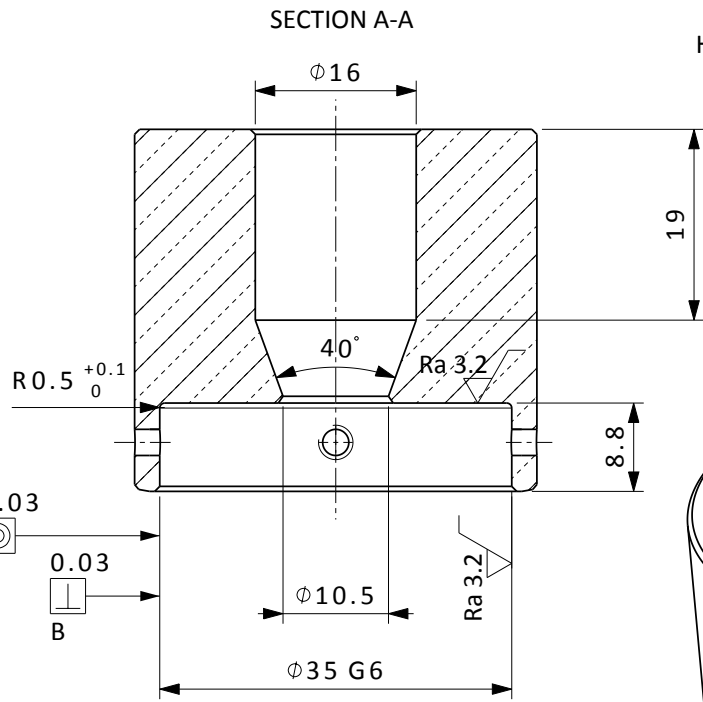
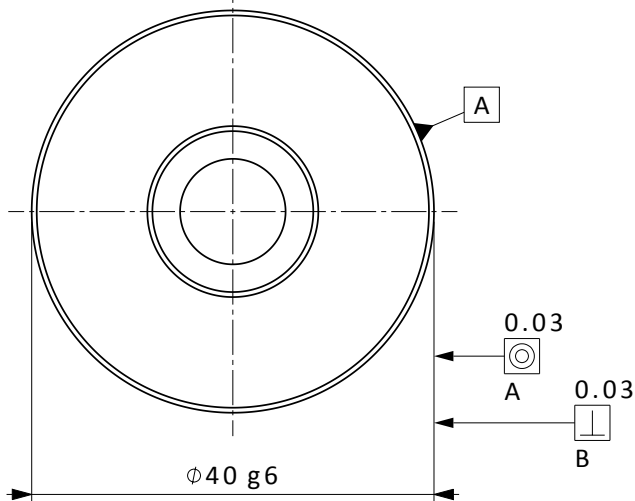
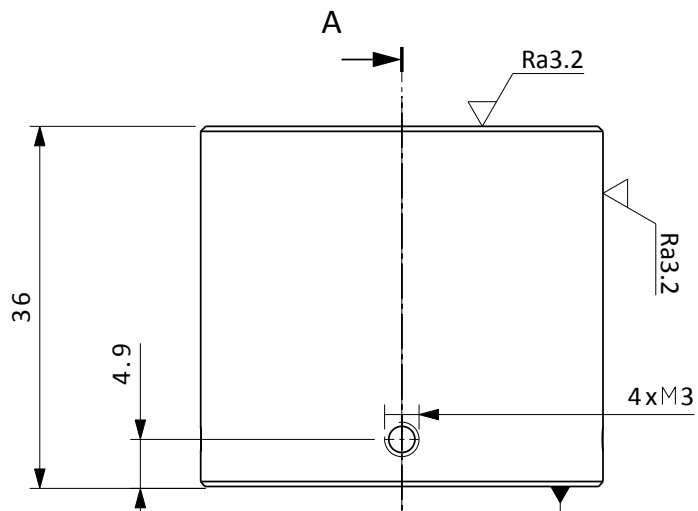


		50x50x20	-	- kg			
PART #	MATERIAL	RAW SIZE	STANDARD/SUPPLIER		WEIGHT		
<b>ASSY WEIGHT: - kg</b>		DRAWING TYPE; TITLE; SUPPLEMENTARY TITLE					
General Tolerances		Final Machining Drawing					
Linear Dimensions, Form and Position:		<b>Lower Seat</b>					
Chamfers, Radii and Angular Dim's:		Machine Drawing Lower Seat					
SURFACE FINISH Min. Ra 3.2		MODELED BY	DATE	DRAWING NUMBER			
Documentation protection as per <b>ISO 16016</b>		martinedung	17/01/2017	ESS-0092318			
 EUROPEAN SPALLATION SOURCE  DESIGN SITE ESS Lund		DRAWN BY	DATE	LIFECYCLE LABEL	REV.	SHEET	
		CHECKED BY	DATE			1/1	
		APPROVED BY	DATE				
		QUALITY CONTROLLED BY	DATE	LEVEL OF MATURITY	MC	SIZE	SCALE
				M4	A3	2:1	
Produced to <b>ISO 1101, 8015 and 1302</b>							

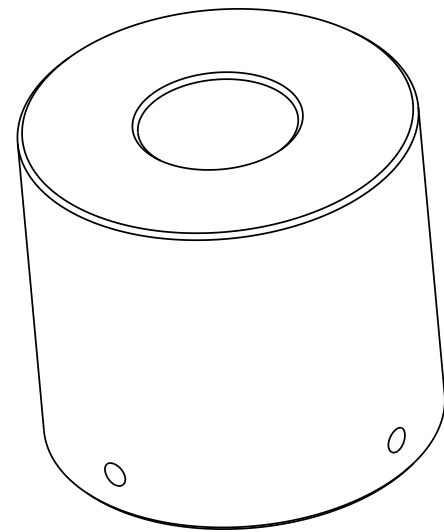




		H=20, D=50			
<b>PART #</b>	<b>MATERIAL</b>	<b>RAW SIZE</b>	<b>STANDARD/SUPPLIER</b>		<b>WEIGHT</b>
<b>ASSY WEIGHT: - kg</b>		DRAWING TYPE; TITLE; SUPPLEMENTARY TITLE			
<b>General Tolerances</b>		Final Machining Drawing			
<b>Linear Dimensions, Form and Position:</b>		<b>Upper Seat</b>			
<b>Chamfers, Radii and Angular Dim's:</b>		<b>Machine Drawing Upper Seat</b>			
<b>SURFACE FINISH</b> Min. Ra 3.2		MODELED BY	DATE	DRAWING NUMBER	
Documentation protection as per <b>ISO 16016</b>		martinedung	12/01/2017	ESS-0092041	
		DRAWN BY	DATE	LIFECYCLE LABEL	REV.
		martinedung	13/01/2017	Preliminary	1.0
		CHECKED BY	DATE	SHEET	1/1
		APPROVED BY	DATE	LEVEL OF MATURITY	MC
		DESIGN SITE		SIZE	A3
		ESS Lund		SCALE	2:1
		QUALITY CONTROLLED BY	DATE	Produced to <b>ISO 1101, 8015 and 1302</b>	



Heat treatment: AT(TF00)



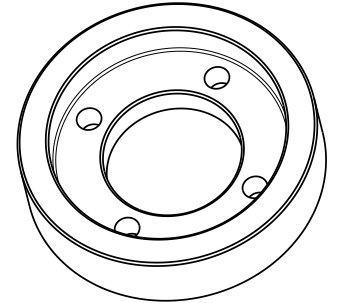
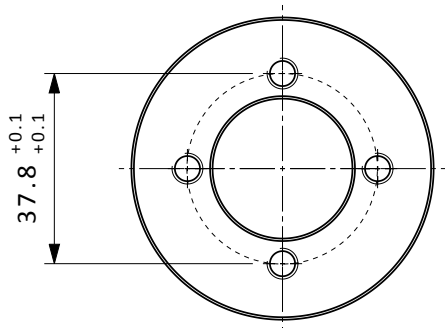
		H=50, D=60		
<b>PART #</b>	<b>MATERIAL</b>	<b>RAW SIZE</b>	<b>STANDARD/SUPPLIER</b>	
<b>ASSY WEIGHT: - kg</b>		DRAWING TYPE; TITLE; SUPPLEMENTARY TITLE		
<b>General Tolerances</b>		Final Machining Drawing		
Linear Dimensions, Form and Position:		Spacer		
Chamfers, Radii and Angular Dim's:		Spacer Drawing		
SURFACE FINISH Min. Ra 3.2		MODELED BY	DATE	DRAWING NUMBER
Documentation protection as per ISO 16016		martinedung	21/12/2016	ESS-0091971
		DRAWN BY	DATE	
		martinedung	13/01/2017	LIFECYCLE LABEL
		CHECKED BY	DATE	REV.
		APPROVED BY	DATE	Preliminary 1.0
		DESIGN SITE	DATE	SCALE
		ESS Lund	DATE	M4 A3 2:1
		QUALITY CONTROLLED BY	DATE	Produced to ISO 1101, 8015 and 1302

4  
3  
2  
1

4  
3  
2  
1

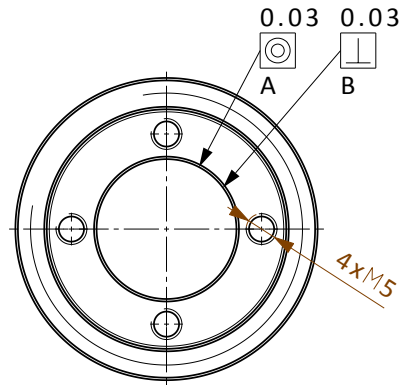
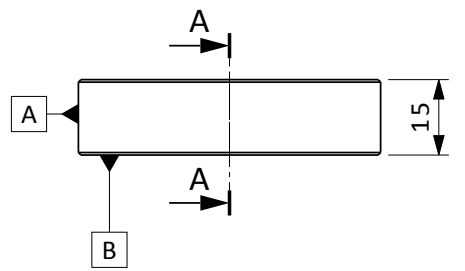
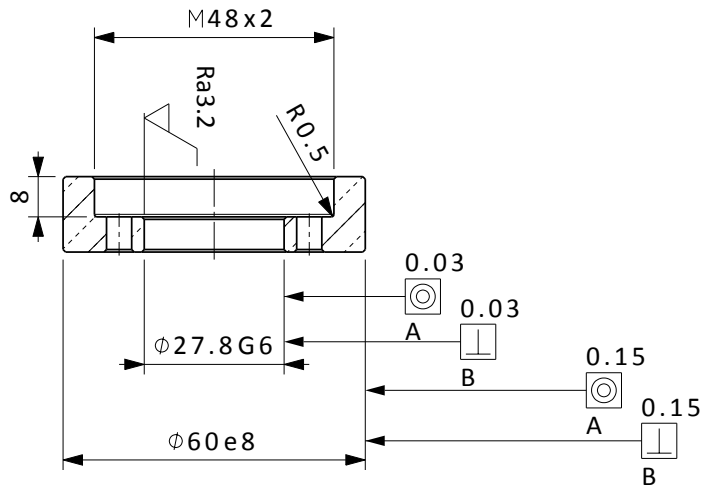
H G F E D C B A

H A



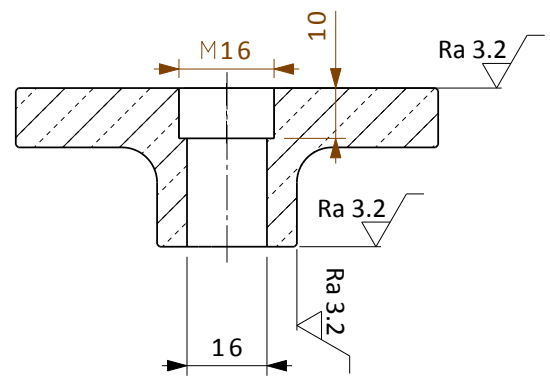
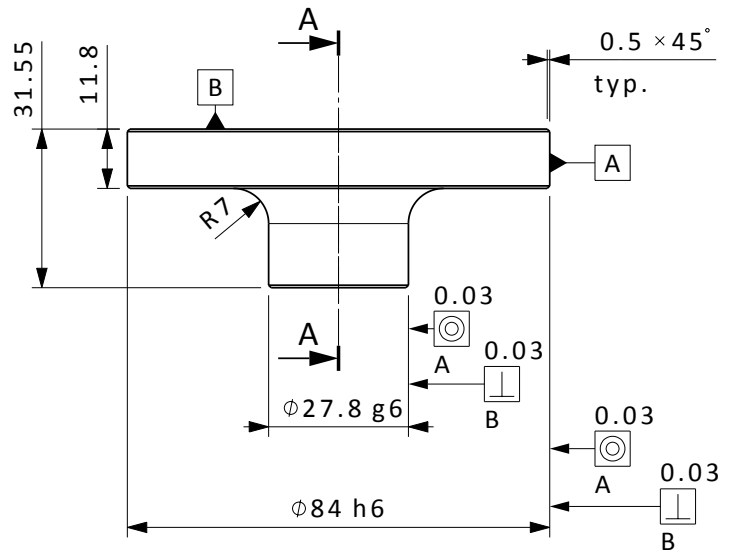
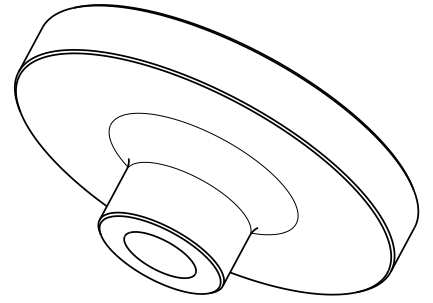
Note: Heat Treatment: AT(TF00)

SECTION A-A

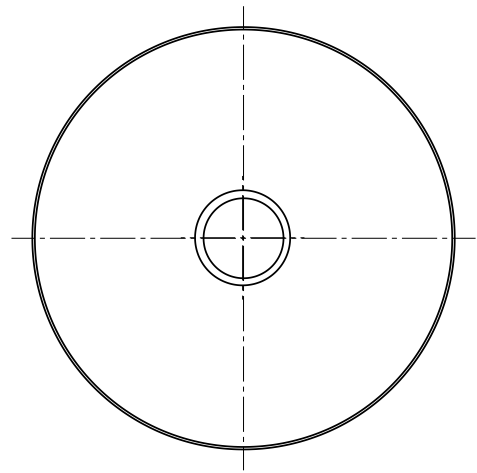



		H=20, D=75		
<b>PART #</b>	<b>MATERIAL</b>	<b>RAW SIZE</b>	<b>STANDARD/SUPPLIER</b>	
<b>ASSY WEIGHT: - kg</b>		DRAWING TYPE; TITLE; SUPPLEMENTARY TITLE		
<b>General Tolerances</b>		Final Machining Drawing		
Linear Dimensions, Form and Position:		<b>ISO 2768-mK</b>		
Chamfers, Radii and Angular Dim's:		<b>ISO 2768-vK</b>		
<b>SURFACE FINISH</b> Min. Ra 3.2		Machine Drawing Screw Holder		
Documentation protection as per <b>ISO 16016</b>		MODELED BY	DATE	DRAWING NUMBER
		martinedung	21/12/2016	<b>ESS-0092022</b>
		DRAWN BY	DATE	
		martinedung	13/01/2017	LIFECYCLE LABEL
		CHECKED BY	DATE	REV.
		APPROVED BY	DATE	<b>Preliminary</b>
		QUALITY CONTROLLED BY	DATE	<b>1.0</b>
				SHEET
				<b>1/1</b>
				LEVEL OF MATURITY
				MC
				SIZE
				A3
				SCALE
				1:1
Produced to <b>ISO 1101, 8015 and 1302</b>				

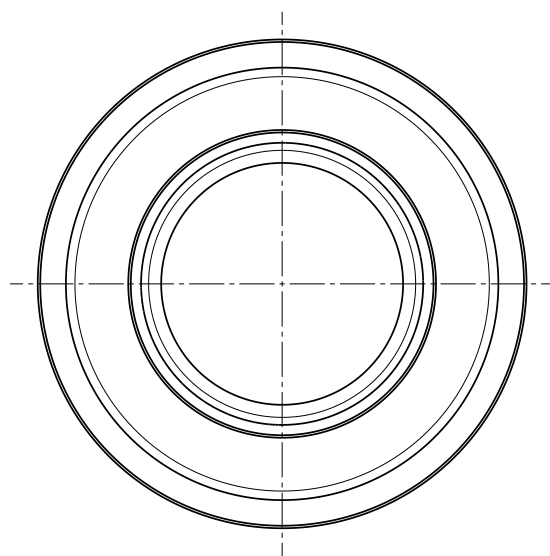
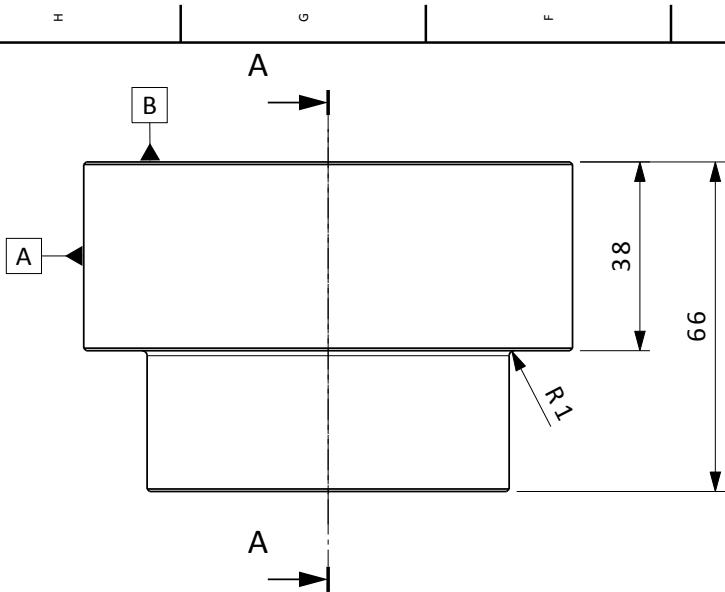




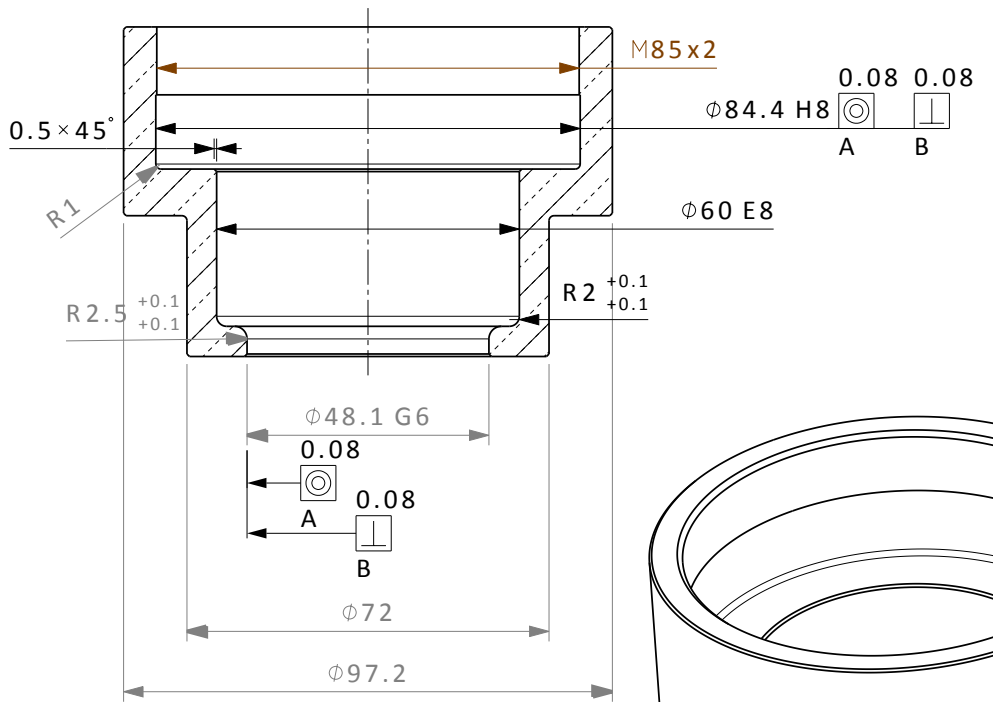
SECTION A-A



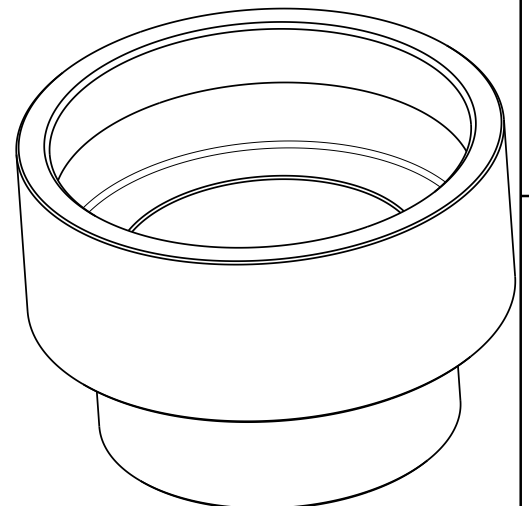
		100x100x40	-	- kg
<b>PART #</b>	<b>MATERIAL</b>	<b>RAW SIZE</b>	<b>STANDARD/SUPPLIER</b>	<b>WEIGHT</b>
<b>ASSY WEIGHT: - kg</b>		DRAWING TYPE; TITLE; SUPPLEMENTARY TITLE		
General Tolerances		-		
Linear Dimensions, Form and Position:		Machine Drawing Piston		
Chamfers, Radii and Angular Dim's:		MODELED BY	DATE	DRAWING NUMBER
SURFACE FINISH Min. Ra 3.2		DRAWN BY	DATE	ESS-0092470
Documentation protection as per ISO 16016		martinedung	18/01/2017	
 EUROPEAN SPALLATION SOURCE		CHECKED BY	DATE	LIFECYCLE LABEL
		APPROVED BY	DATE	REV.
		QUALITY CONTROLLED BY	DATE	SHEET
				Preliminary 1.0 1/1
				LEVEL OF MATURITY MC SIZE SCALE
				Produced to ISO 1101, 8015 and 1302




SECTION A-A

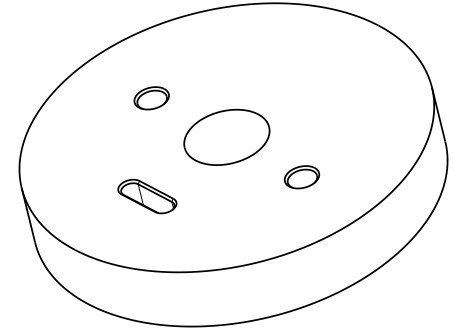
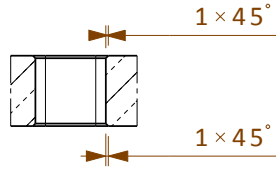


Note: Heat Treatment: AT(TF00)

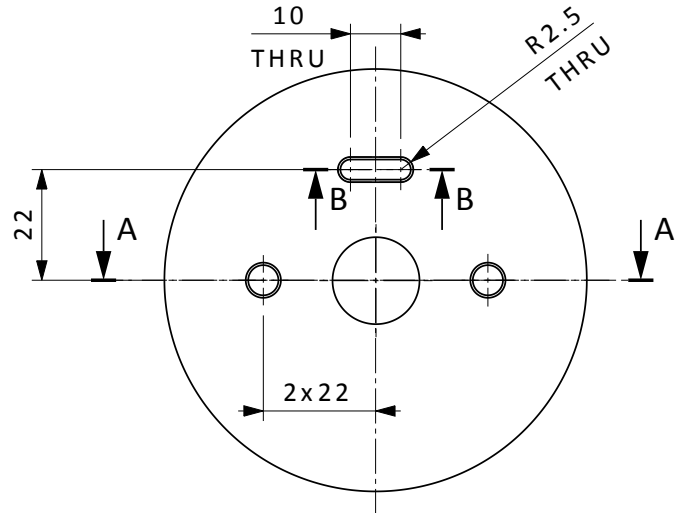


		H=80, D=120		
PART #	MATERIAL	RAW SIZE	STANDARD/SUPPLIER	
<b>ASSY WEIGHT: - kg</b> General Tolerances Linear Dimensions, Form and Position: <b>ISO 2768-mK</b> Chamfers, Radii and Angular Dim's: <b>ISO 2768-vK</b> SURFACE FINISH Min. Ra 3.2 Documentation protection as per <b>ISO 16016</b>		DRAWING TYPE; TITLE; SUPPLEMENTARY TITLE Final Machining Drawing <b>Part 8</b> Machine Drawing Part 8		
 EUROPEAN SPALLATION SOURCE DESIGN SITE ESS Lund		MODELED BY martinedung DATE 11/01/2017	DRAWING NUMBER <b>ESS-0092030</b>	
		DRAWN BY martinedung DATE 13/01/2017	LIFECYCLE LABEL <b>Preliminary</b>	REV. <b>1.0</b>
		CHECKED BY  DATE  APPROVED BY  DATE  QUALITY CONTROLLED BY  DATE	SHEET <b>1/1</b>	SCALE <b>1:1</b>
Produced to <b>ISO 1101, 8015 and 1302</b>				

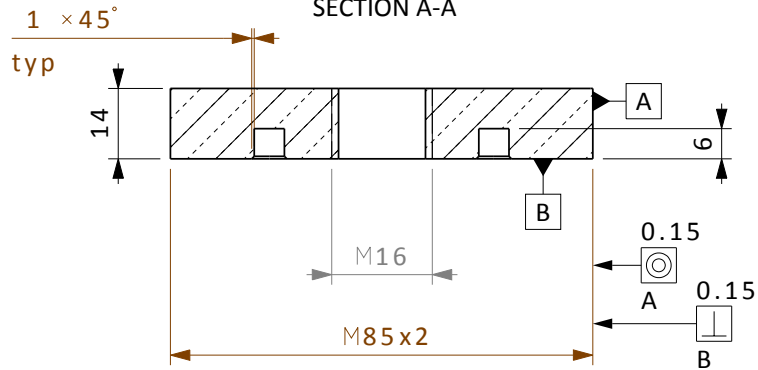
SECTION B-B





Note: Heat Treatment AT(TF00)



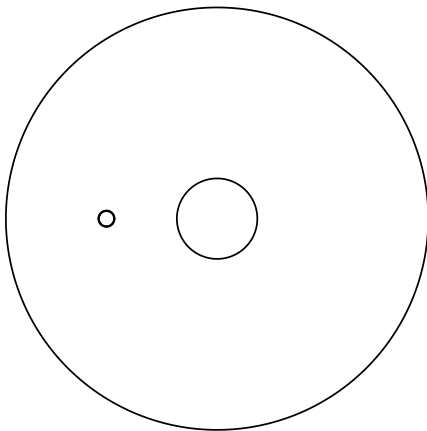
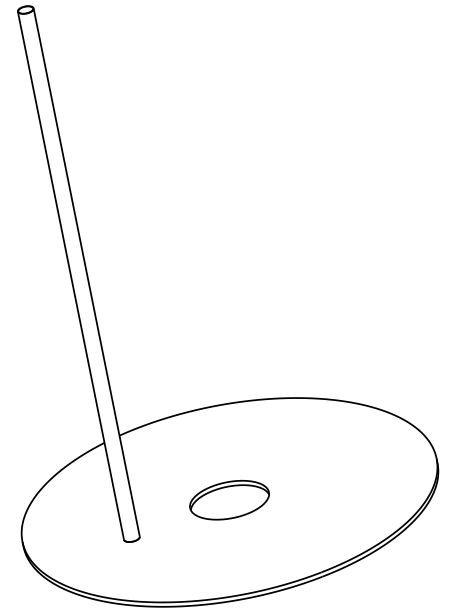
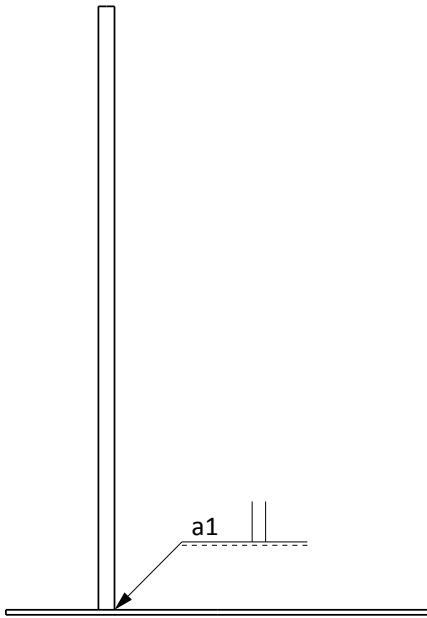
SECTION A-A





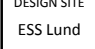
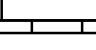

		110x110x20	-	- kg
PART #	MATERIAL	RAW SIZE	STANDARD/SUPPLIER	WEIGHT
<b>ASSY WEIGHT: - kg</b> General Tolerances Linear Dimensions, Form and Position: <b>ISO 2768-mK</b> Chamfers, Radii and Angular Dim's: <b>ISO 2768-vK</b> SURFACE FINISH Min. Ra 3.2 Documentation protection as per <b>ISO 16016</b>		DRAWING TYPE; TITLE; SUPPLEMENTARY TITLE Final Machining Drawing Machine Drawing Threaded Lid MODELED BY _____ DATE _____ DRAWN BY martinedung DATE 18/01/2017 CHECKED BY _____ DATE _____ APPROVED BY _____ DATE _____ QUALITY CONTROLLED BY _____ DATE _____		
 EUROPEAN SPALLATION SOURCE  DESIGN SITE		DRAWING NUMBER <b>ESS-0092471</b> LIFECYCLE LABEL REV. SHEET <b>Preliminary 1.0 1/1</b> LEVEL OF MATURITY MC SIZE SCALE Produced to <b>ISO 1101, 8015 and 1302</b>		

H G F E D C B A

4  
3  
2  
1

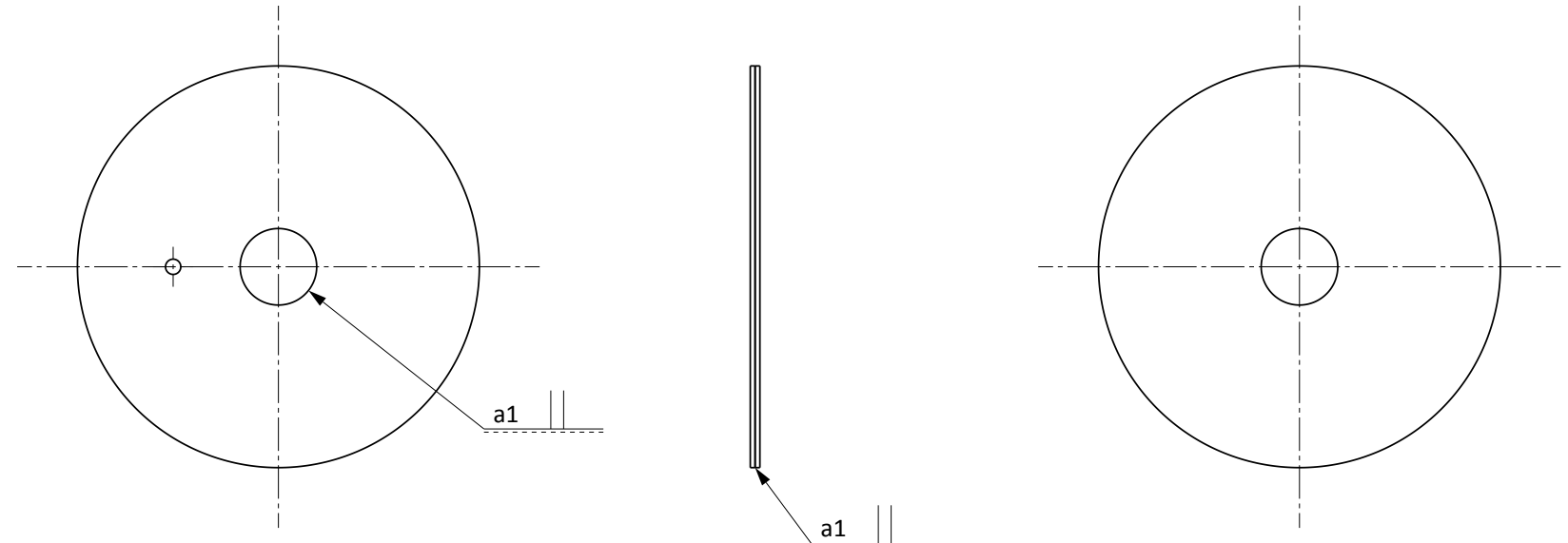


Note: Weld should be leak tight

<b>ASSY WEIGHT:</b> - kg		DRAWING TYPE; TITLE; SUPPLEMENTARY TITLE Weldment Drawing			
<b>General Tolerances</b>		<b>Plate and Straw</b>			
Linear Dimensions, Form and Position:		<b>ISO 2768-mK</b>		Weld Drawing for Inflatable Plate and Straw	
Chamfers, Radii and Angular Dim's:		<b>ISO 2768-vK</b>		MODELED BY	DATE
SURFACE FINISH Min. Ra 3.2		Documentation protection as per <b>ISO 16016</b>		martinedung	18/01/2017
 <b>EUROPEAN SPALLATION SOURCE</b>		 DESIGN SITE ESS Lund		DRAWN BY	DATE
				martinedung	18/01/2017
		CHECKED BY	DATE	DRAWING NUMBER	
				ESS-0092584	
		APPROVED BY	DATE	LIFECYCLE LABEL	REV.
				Preliminary	1.0
		QUALITY CONTROLLED BY	DATE	SHEET	
				1/1	
				LEVEL OF MATURITY	MC
				M4	SIZE
				A3	SCALE
				1:1	
Produced to <b>ISO 1101, 8015 and 1302</b>					

H A

H G F E D C B A



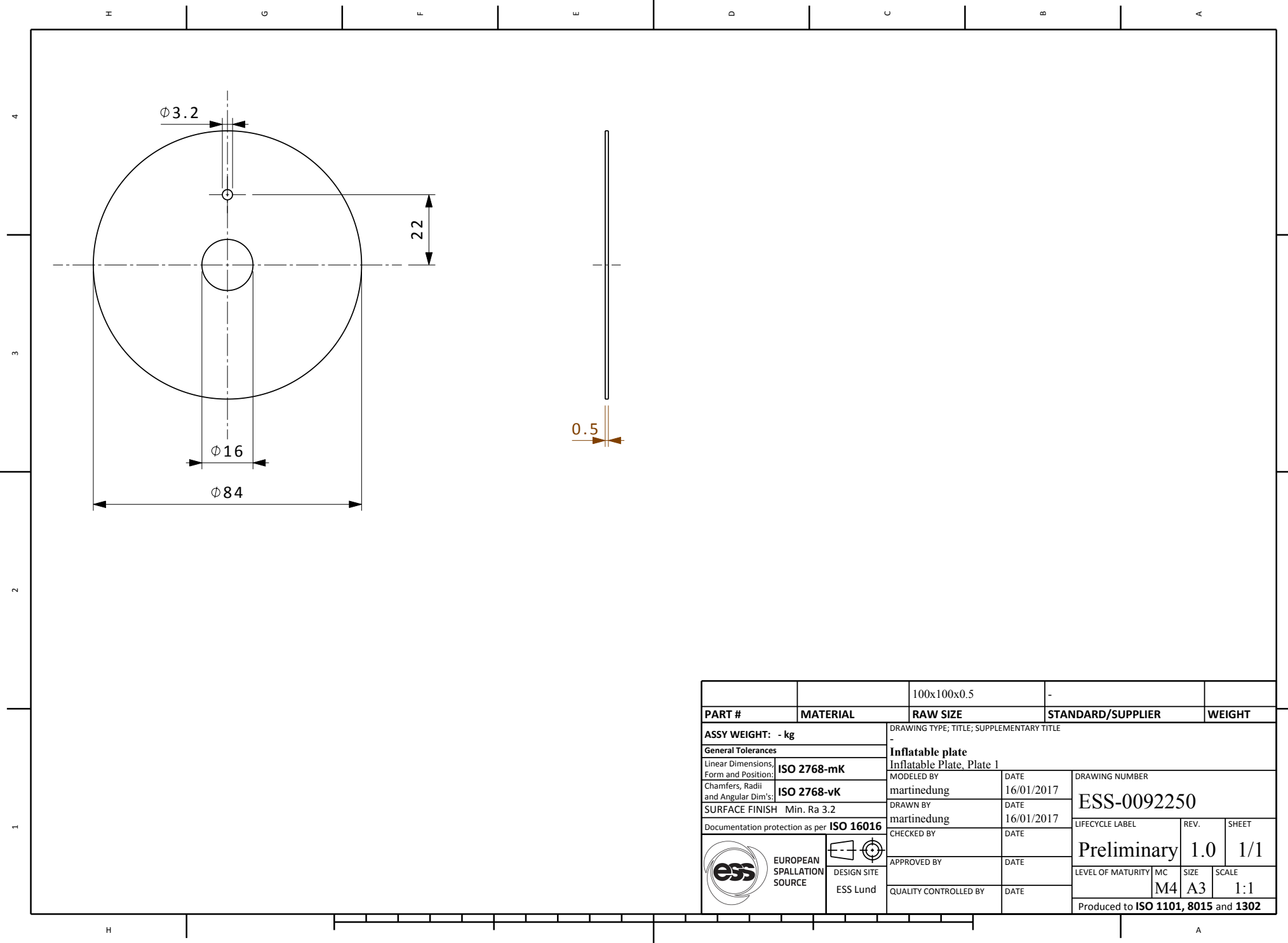
Note: Weld should be Leak Tight



		100x100x2	-	- kg
PART #	MATERIAL	RAW SIZE	STANDARD/SUPPLIER	WEIGHT
<b>ASSY WEIGHT: - kg</b>		DRAWING TYPE; TITLE; SUPPLEMENTARY TITLE		
<b>General Tolerances</b>		Weldment Drawing		
Linear Dimensions, Form and Position: <b>ISO 2768-mK</b>		<b>Inflatable plate</b>		
Chamfers, Radii and Angular Dim's: <b>ISO 2768-vK</b>		Assembly Drawing Inflatable Plate		
SURFACE FINISH Min. Ra 3.2		MODELED BY	DATE	DRAWING NUMBER
Documentation protection as per <b>ISO 16016</b>		martinedung	16/01/2017	<b>ESS-0092251</b>
		DRAWN BY	DATE	
		martinedung	16/01/2017	LIFECYCLE LABEL
		CHECKED BY	DATE	REV.
				<b>Preliminary</b>
		APPROVED BY	DATE	SIZE
				<b>1.0</b>
		QUALITY CONTROLLED BY	DATE	SHEET
				<b>1/1</b>
				LEVEL OF MATURITY MC
				<b>M4</b>
				SCALE
				<b>1:1</b>
Produced to <b>ISO 1101, 8015 and 1302</b>				

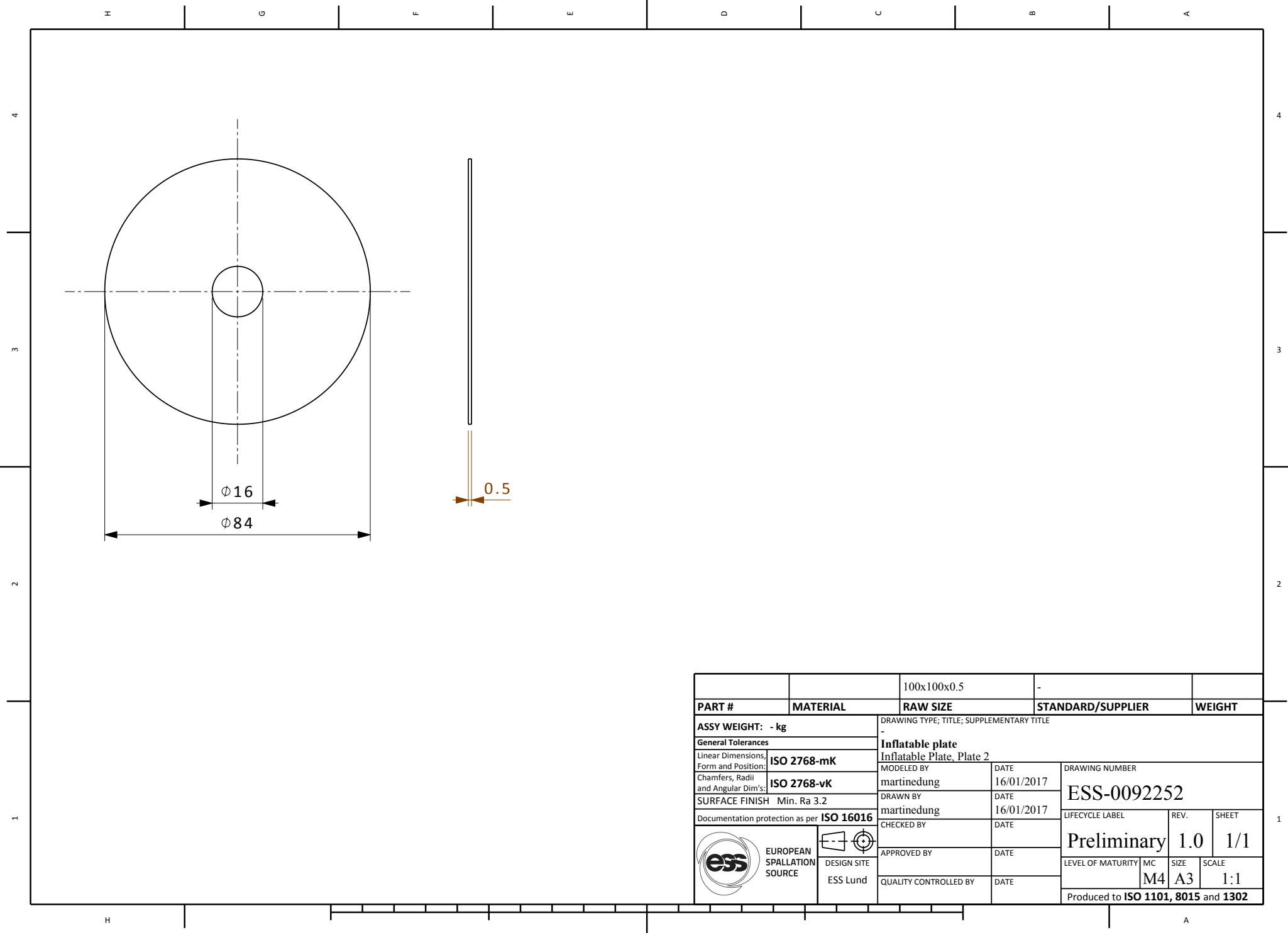



H A





		100x100x0.5	-	
PART #	MATERIAL	RAW SIZE	STANDARD/SUPPLIER	WEIGHT
<b>ASSY WEIGHT: - kg</b> General Tolerances Linear Dimensions, Form and Position: <b>ISO 2768-mK</b> Chamfers, Radii and Angular Dim's: <b>ISO 2768-vK</b> SURFACE FINISH Min. Ra 3.2 Documentation protection as per <b>ISO 16016</b>		DRAWING TYPE; TITLE; SUPPLEMENTARY TITLE - <b>Inflatable plate</b> Inflatable Plate, Plate 1		
 EUROPEAN SPALLATION SOURCE		MODELED BY martinedung	DATE 16/01/2017	DRAWING NUMBER <b>ESS-0092250</b>
 DESIGN SITE ESS Lund		DRAWN BY martinedung	DATE 16/01/2017	LIFECYCLE LABEL <b>Preliminary</b>
		CHECKED BY	DATE	REV. <b>1.0</b>
		APPROVED BY	DATE	SHEET <b>1/1</b>
		QUALITY CONTROLLED BY	DATE	LEVEL OF MATURITY <b>M4</b>
				MC <b>A3</b>
				SIZE <b>1:1</b>
				SCALE <b>1:1</b>
Produced to <b>ISO 1101, 8015 and 1302</b>				



		100x100x0.5	-	
PART #	MATERIAL	RAW SIZE	STANDARD/SUPPLIER	WEIGHT
<b>ASSY WEIGHT:</b> - kg General Tolerances Linear Dimensions, Form and Position: <b>ISO 2768-mK</b> Chamfers, Radii and Angular Dim's: <b>ISO 2768-vK</b> SURFACE FINISH Min. Ra 3.2 Documentation protection as per <b>ISO 16016</b>		DRAWING TYPE; TITLE; SUPPLEMENTARY TITLE - <b>Inflatable plate</b> Inflatable Plate, Plate 2		
 EUROPEAN SPALLATION SOURCE		MODELED BY martinedung	DATE 16/01/2017	DRAWING NUMBER <b>ESS-0092252</b>
DESIGN SITE ESS Lund		DRAWN BY martinedung	DATE 16/01/2017	LIFECYCLE LABEL <b>Preliminary</b>
		CHECKED BY	DATE	REV. <b>1.0</b>
		APPROVED BY	DATE	SHEET <b>1/1</b>
		QUALITY CONTROLLED BY	DATE	LEVEL OF MATURITY <b>M4</b>
				SIZE <b>A3</b>
				SCALE <b>1:1</b>
Produced to <b>ISO 1101, 8015 and 1302</b>				